The Lightning and Dual-Polarization Radar Characteristics of Three Hail-Accumulating Thunderstorms

ROBINSON WALLACE AND KATJA FRIEDRICH

Department of Atmospheric and Oceanic Sciences, University of Colorado Boulder, Boulder, Colorado

WIEBKE DEIERLING

Department of Aerospace Engineering Sciences, University of Colorado Boulder, and National Center for Atmospheric Research, Boulder, Colorado

EVAN A. KALINA

Cooperative Institute for Research in Environmental Sciences, University of Colorado Boulder, and NOAA/Global Systems Laboratory, Boulder, Colorado

PAUL SCHLATTER

National Oceanic and Atmospheric Administration/National Weather Service, Boulder, Colorado

(Manuscript received 30 October 2019, in final form 25 May 2020)

ABSTRACT

Thunderstorms that produce hail accumulations at the surface can impact residents by obstructing roadways, closing airports, and causing localized flooding from hail-clogged drainages. These storms have recently gained an increased interest within the scientific community. However, differences that are observable in real time between these storms and storms that produce nonimpactful hail accumulations have yet to be documented. Similarly, the characteristics within a single storm that are useful to quantify or predict hail accumulations are not fully understood. This study uses lightning and dual-polarization radar data to characterize hail accumulations from three storms that occurred on the same day along the Colorado–Wyoming Front Range. Each storm's characteristics are verified against radar-derived hail accumulation maps and in situ observations. The storms differed in maximum accumulation, either producing 22 cm, 7 cm, or no accumulation. The magnitude of surface hail accumulations is found to be dependent on a combination of in-cloud hail production, storm translation speed, and hailstone melting. The optimal combination for substantial hail accumulations is enhanced in-cloud hail production, slow storm speed, and limited hailstone melting. However, during periods of similar in-cloud hail production, lesser accumulations are derived when storm speed and/or hailstone melting, identified by radar presentation, is sufficiently large. These results will aid forecasters in identifying when hail accumulations are occurring in real time.

1. Introduction

Thunderstorms that produce surface hail accumulations can impact residents and businesses by obstructing roadways, closing airports, and causing localized flooding from hail-clogged drainages. While storms that produce hail accumulations, sometimes in excess of 50 cm, have recently gained increased interest in the scientific community (e.g., Schlatter and Doesken 2010; Friedrich et al. 2019), there still exists a lack of knowledge of how to differentiate storms that produce impactful accumulations from those that produce only scattered hail. Similarly, the characteristics within a single storm that are useful in inferring the quantity of hail accumulation are not fully understood. Consequently, forecasters are unable to provide reliable hail depth information to the public with a sufficient lead time (or in some cases no

Supplemental information related to this paper is available at the Journals Online website: https://doi.org/10.1175/WAF-D-19-0224.s1.

Corresponding author: Robinson Wallace, robinson.wallace@colorado.edu

DOI: 10.1175/WAF-D-19-0224.1

lead time at all) that may mitigate storm impacts. To provide valuable insight into the contributing factors that characterize hail-accumulating storms, we investigated three individual hailstorms that occurred on the same day along the Colorado–Wyoming Front Range. Each storm produced a maximum accumulation of 22 cm, 7 cm, or no accumulation. In conjunction with operational lightning and dual-polarization radar data, we addressed the following questions: How does the evolution of microphysical and kinematic processes differ in each storm? Can a select combination of these processes be used to identify areas of significant hail accumulation? And, how much lead time can forecasters gain by tracking a storm's evolution?

Even though hail-accumulating storms have been documented for over a century (Schlatter and Doesken 2010), the economic and life-threatening effects of such thunderstorms have surprisingly only recently begun to garner the increased interest of government and academic organizations. Along the Colorado–Wyoming Front Range, numerous occurrences of hail accumulations larger than 3 cm in depth have been reported by the public in recent years (Kalina et al. 2016; Friedrich et al. 2019; Wallace et al. 2019). As referenced in Wallace et al. (2019), even shallow accumulations of roughly 3 cm have closed the Denver International Airport, resulting in millions of dollars lost to the local economy for each hour the airport remained closed. Larger accumulations on highways have been identified as costing hundreds of thousands of dollars in economic and emergency response cost. The impacts to life and property attributed to hail accumulations have been documented not just in the immediate Colorado–Wyoming area (Durta 2016), but also elsewhere in the United States (Ward et al. 2018; Kumjian et al. 2019) as well as locations in Europe, Central America, and South America (Kroosec 2013; Samenow 2014; Lawrence 2017). When considering the impacts of hail-accumulating storms, it is clear there exists a need to understand these storms in detail.

One detail that may be important to understanding hail-accumulating thunderstorms is what conditions are necessary for their development. Necessary for all organized convection is a mechanism for lift, an unstable atmosphere, wind shear, and available moisture (e.g., Doswell 1987; Brooks et al. 2003). These can be inferred from the large-scale environment. However, on a more local scale, the amount of storm-scale hail production may depend strongly on the storm relative wind and wind shear profiles, as well as humidity profiles, and the presence of hailstone embryos (e.g., Grant and van den Heever 2014; Johnson and Sugden 2014; Dennis and Kumjian 2017). Notably, when used alone, many of these variables have been shown to be poor discriminators of hail size (Johnson and Sugden 2014). The best discriminators of hail size have been found to use multiple variables in tandem (Johnson and Sugden 2014; Allen et al. 2020). But it is still unclear if it is possible to use single or combinations of variables to lend insight into what conditions can help differentiate storms that do and do not produce hail accumulations. Unfortunately, the near-storm-scale variability presents difficult challenges to measure its effects on hail accumulations due to inadequate in situ observations. Due to that difficulty, we do not address the effects of the near-storm environments this study. However, the preconvective mesoscale variability is measurable through radiosonde observations, making addressing its effects possible. It should be said that more research is necessary to understand how the mesoscale and near-storm-scale variability plays a role in hail accumulations.

While the mesoscale variability may be important, identifying such storms is also dependent on understanding each storm's real-time inferable characteristic physical processes. Unfortunately, for the efforts to understand such processes, the majority of the literature focuses on understanding the physical processes necessary for in-cloud hail growth, and not those that govern the amount of hail accumulation on the ground. Some insight has recently been gained about hailstorms that produced more than 10 cm of accumulation (Kalina et al. 2016; Friedrich et al. 2019; Kumjian et al. 2019). The evidence suggests the amount of hail accumulation may depend on a combination of three primary storm characteristics: storm motion, hailstone melting rates, and in-cloud hail production. However, it is not known how each of these characteristics affect a storm's potential for producing hail accumulations.

It might be intuitive that storms that produce the deepest hail accumulations move slower and occur in environments prohibitive to melting. When addressing the impact of storm motion, four hail-accumulating thunderstorms studied by Kalina et al. (2016) were on average slower than the climatological norm. Contrary to their results, recent research has found storm motions that exceeded the climatological norm and still produced accumulations greater than 10 cm (Friedrich et al. 2019; Kumjian et al. 2019). This discovery suggests storm motion itself is not necessarily a reliable indicator of the maximum hail accumulation. The maximum accumulation is also hypothesized to be dependent on the rate that hailstones are melting. If the melting rate is substantial enough, the stones will be reduced to rain prior to reaching the surface. Smaller melting rates may instead reduce or yield no effect on the maximum accumulation. However, contrary to this hypothesis, it is possible that substantial melting existed in hail-accumulating storms where accumulations exceeded 10 cm. These storms exhibited warm and humid environments conducive to melting, as evidenced by large rain rates (90 mm h^{-1}) or large amounts of cloud liquid water content indicated from the radar-derived specific differential phase ($K_{DP} > 7° km^{-1}$; Chappell and Rogers 1988; Schlatter and Doesken 2010; Ward et al. 2018; Kumjian et al. 2019). As a result, the importance of the role that hailstone melting plays in hail-accumulating storms is still unknown.

The last characteristic provided in our hypothesis is the importance of in-cloud hail production. In-cloud hail production is tied to three storm characteristics (e.g., Browning 1964; Browning and Foote 1976; Conway and Zrnić 1993; Dennis and Kumjian 2017): (i) the storm must develop an updraft with a sufficient strength and width to suspend hailstones/embryos within temperatures conducive to hailstone growth, (ii) ample amounts of supercooled liquid water must be present to allow for optimal growth, and (iii) the quantity of hail produced depends on the concentration of hailstone embryos within the updraft. Strong updrafts can be inferred by tracking storm-top divergence (Witt and Nelson 1991; Blair et al. 2011) and identifying areas of radar-derived positive differential reflectivity Z_{DR} columns extending above the melting level (e.g., Bringi et al. 1991; Conway and Zrnić 1993; Hubbert et al. 1998; Kumjian and Ryzhkov 2008; Kumjian et al. 2014). These positive Z_{DR} columns indicate the presence of liquid water droplets being lifted into areas of subfreezing temperatures and enhanced accretion. As a result, deep and long-lived Z_{DR} columns may result in enhanced hail production compared to storms with shallower, short-lived, or no Z_{DR} columns (Kumjian et al. 2014). Another avenue to infer strength and width of updrafts involves assessing trends in lightning activity. In particular, flash extent density (defined as the number of flashes that cross a column per unit time) and the convex-hull area of each flash (defined as the average flash area to occupy a column each time step, referred to henceforth as flash footprint) correlate to updraft volume, location, and to a lesser extent, maximum updraft speed (Baker et al. 1999; Rutledge et al. 1992; Williams et al. 1999; Deierling and Petersen 2008; Bruning and MacGorman 2013; Calhoun et al. 2013; Zheng and MacGorman 2016; Schultz et al. 2015). Recent work suggests that turbulent motions in storms may control the distribution of charge regions, which in turn relate to flash sizes (e.g., Bruning and MacGorman 2013; Calhoun et al. 2013; Brothers et al. 2018). These turbulent motions in and around thunderstorm updrafts may create small pockets of charge regions favoring more frequent but smaller flashes surrounding the updraft. As a result, the density of flashes can increase while the average footprint may decrease when updrafts are intensifying.

Hail production is also dependent on the cloud water and ice content. Radar products such as vertically integrated ice (VII; Carey and Rutledge 2000; Gauthier et al. 2006; Mosier et al. 2011) are intended to provide information about the amount of supercooled water and ice content within the cloud and can be used as a proxy for in-cloud hail production (Friedrich et al. 2019). Similarly, dual-polarization radar variables can provide evidence of mixed-phased precipitation, supercooled water, and ice in clouds (e.g., Balakrishnan and Zrnić 1990b; Zrnić et al. 1993; Brandes et al. 1995; Hubbert et al. 1998). Water and ice cloud contents are related to lightning activity, as charge separation depends on rebounding ice hydrometeor collisions in the presence of supercooled water (Takahashi 1978; Saunders 1993). Enhanced flash activity is indicative of more frequent ice collisions and, therefore, larger quantities of in-cloud ice and water content (e.g., Deierling et al. 2008; Lund et al. 2009; Calhoun et al. 2013; Schultz et al. 2015).

In addition to updraft strength and width and supercooled liquid water amounts, the quantity of hailstone embryos is important to the rate of hail production (e.g., Conway and Zrnić 1993; Hubbert et al. 1998). Unfortunately, hailstone embryos themselves cannot be easily distinguished from cloud droplets by S-band weather radars or trends in lightning activity. While radar-derived proxies (e.g., Z_{DR} columns, bounded weak echo regions) can identify potential hail embryo source regions and embryo curtains (Browning 1964; Browning and Foote 1976; Nelson 1983; Conway and Zrnić 1993; Knight and Knight 2001; Tessendorf et al. 2005), differences in radar geometry makes comparing these features across storms difficult. Thus, we refrained from investigating the influence of hailstone embryos in this study.

In this study we investigated the storm motion, hailstone melting, and hail production in three separate thunderstorms that occurred on 5 June 2015 in the Denver, Colorado, metro area. Reported hail accumulations ranged from >20 cm in depth to scattered hail (i.e., no measurable depth) (squares in Fig. 1). We utilized operational lightning and dual-polarization radar data to investigate the spatiotemporal evolution of the updraft, liquid water, and cloud ice content of each storm through their life cycle. By investigating each storm characteristic independently as well as in tandem, we show patterns that are useful to identify areas of accumulating hail in each storm. Importantly, because each storm occurred within 6 h of each other, the influence of the large-scale atmospheric environment on the results was mitigated. Ultimately, this research will provide a valuable avenue toward identifying useful

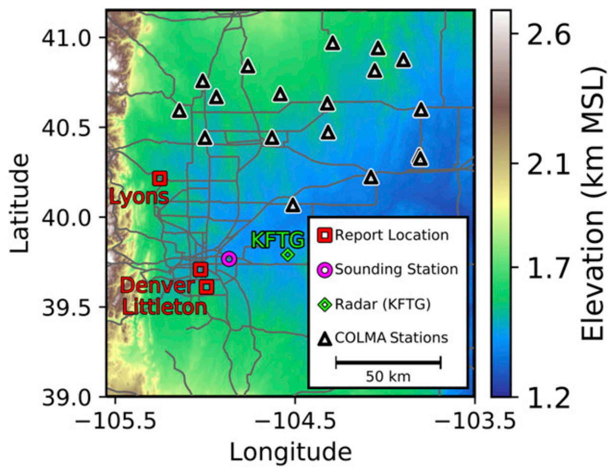

FIG. 1. Map of the study area. Also shown are the hail depth report and instrument locations used in this study. Major roads are in gray.

information for forecasters and emergency personnel in terms of discussing the spatial and temporal evolution of radar and lightning parameters and how they relate to the depth and distribution of hail accumulations at the surface.

2. Instruments and methods

a. Radar data

For this study, we used data collected by the operational Weather Surveillance Radar-1988 Doppler (WSR-88D) in Denver (KFTG; Fig. 1). Data were obtained between 2300 UTC 4 June 2015 and 0800 UTC 5 June. The data were kept in polar coordinates to provide the most useful information, thereby avoiding approximations made during interpolation to Cartesian coordinates. Except in the analysis of Z_{DR} column height and VII, radar grid cells were limited to the lowest elevation scan and to cells identified as hail or hail-with-rain by the National Center for Atmospheric Research's hydrometeor classification algorithm (HCA; Vivekanandan et al. 1999). These quality-controlled radar data were used to quantify hail accumulation at the surface, in-cloud hail production, and hailstone melting. While the methods to quantify hail production, storm speed, and melting are explained in this section, we refer the reader to Friedrich et al. (2019) and Wallace et al. (2019) for more information on how we computed radar-derived hail accumulation.

Hail production was inferred using three derived products: (i) vertically integrated ice (VII), (ii) storm-top divergence, and (iii) Z_{DR} column height above the 0°C isotherm. VII was calculated following Mosier et al. (2011). Their method uses Z between the $-10°$ and $-40°$C isotherms to calculate the integrated ice content in a column. Storm-top divergence was derived using a similar method as outlined in Blair et al. (2011). Their method defines storm-top divergence as the sum of the absolute values of the minimum and maximum radial velocity values within 30 km of the divergence region at or near the height of the 50-dBZ echo top. We deviated from their method by only including data within 10 km of each other.

To determine Z_{DR} column heights, we used a manual inspection of Z_{DR} fields. An objective algorithm is provided by Snyder et al. (2015), but we chose not to utilize their algorithm due to the numerous limitations. Of those limitations, particularly concerning for this study are the effects from Z_{DR} calibration errors, low vertical resolution of which can hide small Z_{DR} columns, and three-body scattering. Our first step to manually determine Z_{DR} column height was to minimize noise in the Z_{DR} fields by averaging across five range gates using a Gaussian function (Snyder et al. 2015). Second, for each radar volume, a constant-altitude plan position indicator (CAPPI) was made at the height of the 0°C isotherm. To identify the height of the 0°C isotherm, we used the 2300 UTC 4 June 2015 Rapid Refresh model (RAP; Benjamin et al. 2016) derived sounding closest to the hail depth report location. The 2300 UTC sounding was closest in time to the times of each hail depth report that did not show cooling at the surface, an indication that convection was present. We note that the 0°C isotherm height of 590 hPa measured by the radiosonde launched from Denver at 1200 UTC 4 June 2015 nearly matches the RAP data from 2300 UTC 4 June 2015. We then used the CAPPI to identify areas of enhanced Z_{DR} ($\geq$1 dB) near the locations where hail accumulated based on the radar-derived hail maps. Next, we generated a vertical cross section extending along a series of azimuths that intersected the area of enhanced Z_{DR} most relevant to the accumulations of interest. From each cross section, the largest distance the 1-dB contour extended above the 0°C isotherm was approximated and recorded for that radar volume.

Storm speed was derived using the Level 3 radar product Storm Tracking Information (STI; Johnson et al. 1998). STI derives the latitude and longitude of a storm's centroid for each radar volume using an algorithm based on horizontal and vertical gradients in reflectivity. Through this method, the storm centroid was most commonly placed within the areas of the strongest precipitation rates. It was especially unlikely for the centroid to be placed in areas of updrafts where weak echo regions yielded nonpreferred reflectivity gradients for the STI algorithm. Nonetheless, the precipitation core acted as a valuable location to track and calculate the storm speed. To calculate storm speed, the quotient of the distance change between two successive storm centroids and the change in time between radar scans gave an estimated speed in each radar volume. Because the storm centroid was derived algorithmically, the STI placement of the storm may vary from where a subjective manual inspection may place it using a similar method as used by the STI algorithm. To be as objective as possible, and to reconcile any differences, we smoothed the storm speed using a 1–3–1 weighted average across three observations. This was accomplished by using a running average across three timesteps where the current time step was weighted by multiplying the storm speed by three.

Hailstone melting was inferred by using Z, Z_{DR}, total differential phase Φ_{DP}, and the cross-correlation coefficient R_{HV} from the Level 2 radar data. We derived K_{DP} from Φ_{DP} using NCAR's Radx C++ software package. Specific differential phase K_{DP} was computed by applying a finite impulse response filter with a length of 10 range gates iteratively applied to Φ_{DP} one time to smooth it. A similar method was used by Kumjian et al. (2019). Because K_{DP} strongly depends on the number of gates over which the filter is applied (see Ryzhkov et al. 2005; Kalina et al. 2016; Kumjian et al. 2019; for different approaches), different methods will produce a range of possible melting rates. As a consequence, for this study we used K_{DP} to qualify relative melting between locations, and not to specifically quantify melting rates. For more information on dual-polarization products and their contributions to identifying hailstone characteristics, we refer the reader to Kumjian (2013) and the references therein.

b. Lightning data

To take advantage of the connections between ice production and lightning activity we used data collected from the Colorado Lightning Mapping Array (COLMA; Rison et al. 2012). The 21 stations that compose COLMA are sensitive to very high frequency (VHF) radiation of around 60 MHz (triangles in Fig. 1). This frequency is strongly emitted by charge breakdowns responsible for lightning flashes. COLMA can detect lightning sources up to 350 km away from the array center (Rison et al. 2012). The maximum distance between the array center and the furthest storm in this study is roughly 100 km.

Individual VHF sources were processed with the Lightning Mapping Array (LMA) Tools flash creation algorithm to filter noise and to aggregate the remaining sources into individual lightning flashes (Bruning 2015). Sources were assumed to be part of the same lightning flash if they satisfied the same temporal and spatial criteria as used by Bruning and MacGorman (2013). That is, sources must have occurred within 0.15 s and within 3 km of each other to be grouped into the same flash.

To further filter the raw source data, we specified that grouped sources identified as one flash did not last longer than 3 s. To reduce noise, sources with arrival times that had reduced chi-square goodness of fit values of more than 2.0 were excluded. Finally, each source must have been observed by at least six stations. Once all sources were grouped into flashes, the data were gridded to 1 km $\times$ 1 km grid cells with 1-min temporal resolution. From the fully processed data, the column-derived flash extent density (flashes km^{-2} min^{-1}) and the column average flash footprint (km^2) were computed.

3. Synoptic overview 4 June 2015

At 1200 UTC 4 June, an upper-level trough was present over the West Coast of the United States at 500 hPa, with the axis aligned southwest to northeast (Fig. 2). As a result, anticyclonic southwesterly winds supported large-scale ascent over the Denver region. Also observed over the Denver area were 500-hPa wind speeds that ranged from 8 to 20 m s^{-1} (15–38 kt) with 18 m s^{-1} (35 kt) directly over Denver. A narrow area of dewpoint temperature depressions of less than 25°C at and northeast of Denver indicate that increased midlevel relative humidity was passing through the study region.

The surface analysis shows a stationary front developed as oriented north–south along the eastern edge of the Rocky Mountains by the evening of 4 June (Fig. 3). The Denver area was dominated by a postfrontal air mass that originated from a cold front passing over Denver on 3 June. Cyclonic flow at the surface produced easterly upslope winds of 5–10 m s^{-1}. Ample surface moisture, shown by dewpoint temperatures ranging from 7.2° to 17.2°C (45°–63°F), provided conditional instability to support afternoon convection along the Colorado Front Range (Phillips 1973; Hubbert et al. 1998; Chappell and Rogers 1988).

The operational radiosonde launched at 1200 UTC 4 June from Denver (Fig. 1, circle) also indicates an atmosphere that classically supports strong convection (Fig. 4a). A deep but weak inversion extended from the surface to 700 hPa with conditionally unstable air above the inversion. Winds were observed to rotate clockwise with height until roughly 650 hPa. Above 650 hPa, the winds were unidirectionally from the southwest until 350 hPa when winds began to rotate counterclockwise. Column integrated precipitable water was 17.7 mm, exceeding the 75% climatological normal for 4 June in Denver of 14.2 mm.[1] Surface-based convective available potential energy (CAPE), bulk Richardson number

[1] https://www.spc.noaa.gov/exper/soundingclimo/#.

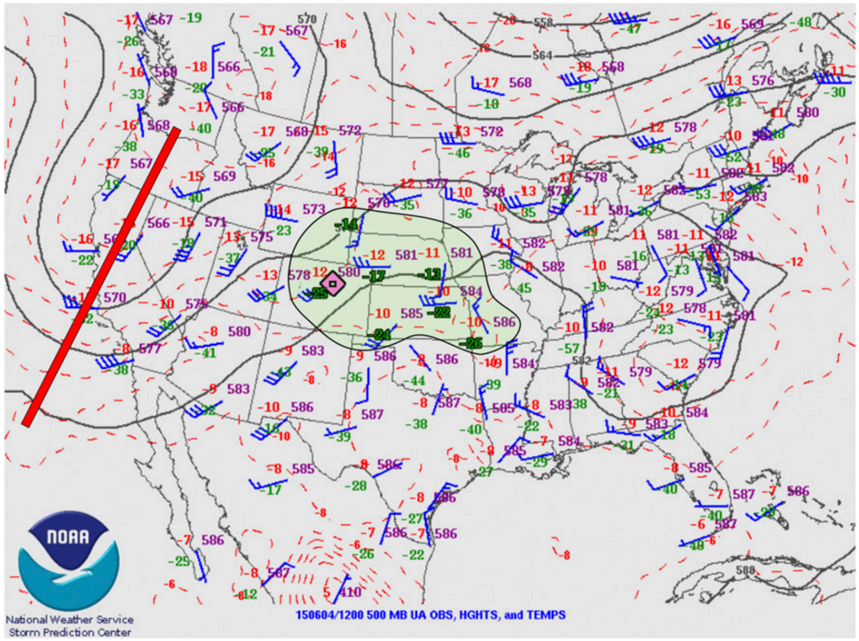

FIG. 2. The 500-hPa map at 0000 UTC 5 Jun 2015. Black contours are geopotential heights, red contours are temperature (°C), and wind barbs (kt) are in blue. Denver is indicated by a pink diamond. The area of small dewpoint depressions is highlighted in green. The upper-level trough is annotated with a red line.

(BRN), bulk shear (0–6 km), and mean winds (0–6 km) were 1425 J kg^{-1}, 59.7, 18.6 m s^{-1}, and 12.7 m s^{-1}, respectively (Table 1). These values suggest an environment that supports multicellular and supercell thunderstorms (Weisman and Klemp 1984). The RAP-derived vertical profile shows similar bulk shear and BRN but slightly higher CAPE (161 J kg^{-1} larger) and 4.1 m s^{-1} slower 0–6-km mean winds (Table 1).

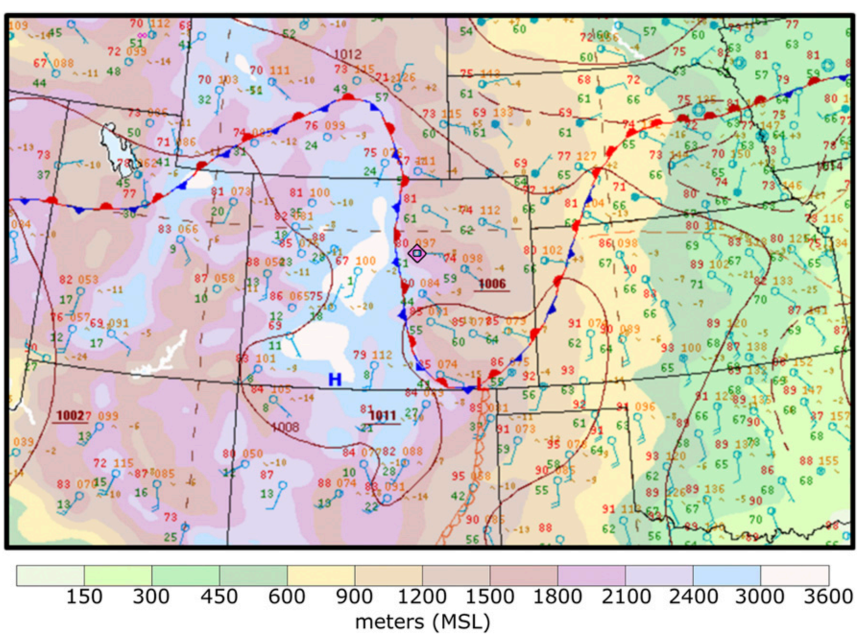

FIG. 3. Surface frontal analysis maps with surface station model plots at 0000 UTC 5 Jun 2015. Color shading indicates terrain height. Black lines show sea level pressure. Denver is indicated by the pink diamond. Image generated at https://www.wpc.ncep.noaa.gov/html/sfc-zoom.php.

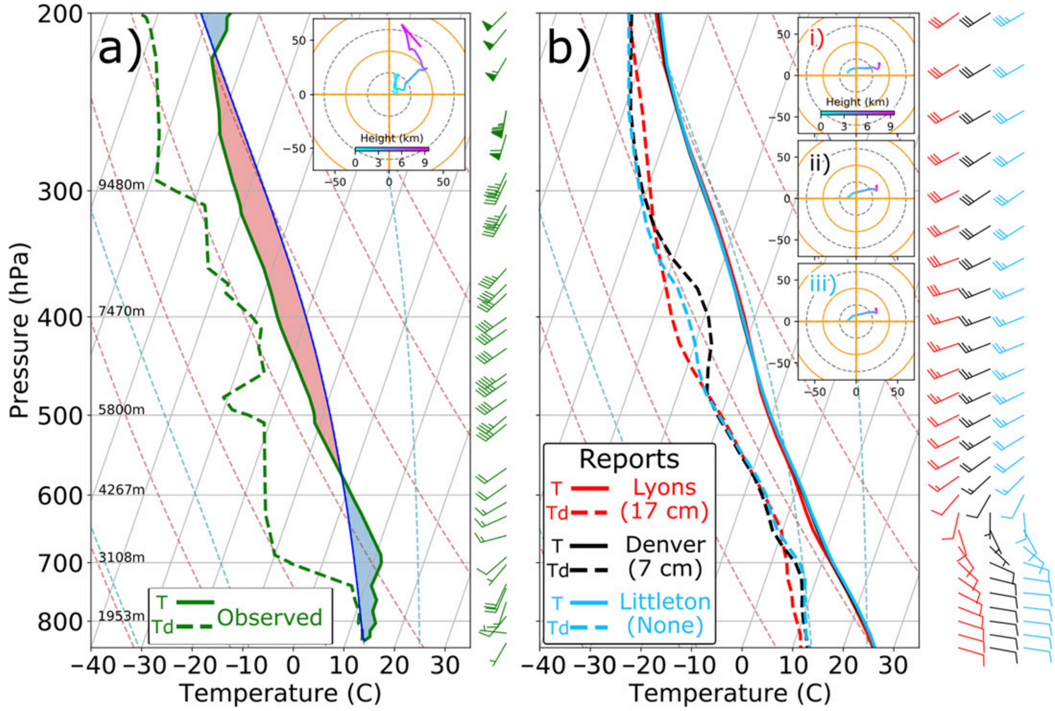

FIG. 4. (a) Observed sounding for 1200 UTC 4 Jun and (b) RAP-derived sounding at the location of each hail depth report at 2300 UTC 4 Jun. Red dashed lines are the dry adiabat, and blue dashed lines are the moist adiabat. Hodographs are located in top right with color coding by height. In (a), heights (m) are shown adjacent to pressure levels, the red shaded region indicates the area of CAPE, and the blue shaded region is the area of CIN.

4. Results

a. *Characteristics of a storm producing deep hail accumulations*

1) PRECONVECTIVE LOCAL ENVIRONMENT

The first storm we analyzed was a supercell thunderstorm that passed over Lyons, Colorado, between 0000 and 0330 UTC 5 June 2015. The storm produced reports of surface hail accumulations greater than 14 cm in depth (visually estimated from photograph by a news-outlet retweet, Fig. 5a) and maximum hail diameters of 5 cm (reported by a storm spotter). At the report location, important changes in the RAP sounding occurred between the observed 1200 UTC [0600 mountain daylight time (MDT)] sounding on 4 June and the 2300 UTC RAP sounding (1700 MDT) on 4 June (Fig. 4, Table 1). An increase in CAPE from 817 to 2357 J kg^{-1} between the morning and afternoon (Table 1) was a result of surface warming from 13° to 24°C. An easterly shift in surface winds resulted in substantial veering winds, and also set up an upslope pattern that was conducive

TABLE 1. Prestorm environments including surface-based convective available potential energy (SBCAPE), bulk Richardson number (BRN), 0–6-km bulk shear, 0–6-km mean winds, and precipitable water derived at 1200 UTC from the operational sounding at Denver, CO, (KDNR) and at 1200 and 2300 UTC from the Rapid Refresh model (RAP). The RAP soundings were derived at KDNR and the location of each hail depth report.

KDNR location at 1200 UTC	SBCAPE (J kg^{-1})	BRN	0–6 km-bulk shear (m s^{-1})	0–6-km mean winds (m s^{-1})	Precipitable water (mm)
Observed	1425	60	18.6	12.7	17.7
RAP	1586	58	19.6	8.6	17.7
Report location at 1200, 2300 UTC (maximum accumulation)					
Lyons (>20 cm)	817, 2357	38, 82	20, 19	7.2, 4.1	13.5, 19.9
Denver (7 cm)	1326, 2891	47, 104	19, 18	9.0, 3.6	14.4, 21.2
Littleton (1 cm)	1483, 2850	53, 112	18, 18	9.6, 3.4	14.2, 22.0

FIG. 5. Photographs showing hail accumulations on 5 Jun at (a) 0330 UTC in Lyons (credit: Valerie Deats), (b) 1400 UTC in Denver (credit: Kathryn Scott/*The Denver Post*), and (c) 0630 UTC in Littleton (credit: Rick Cronenberger).

to storm development. Also notable was a nontrivial moistening in the 750–500-hPa layer that resided in the hail growth zone between 0° and −30°C (Foote 1984). The largest changes occurred at 700 hPa where dewpoint temperatures were 13°C greater at 2300 UTC compared to 1200 UTC. As a consequence, precipitable water increased by 6.4 mm, from 13.5 to 19.9 mm between 1200 and 2300 UTC. The increase in moisture likely contributed to the observed deep accumulations in part because moisture is necessary requirement for hail production. We note, as we show in the following sections, there are multiple factors involved in the resultant depth of accumulation. Below 750 hPa, the layer dried slightly where dewpoint temperatures decreased by 0°–5°C. Finally, the BRN increased from 38 to 82 and 0–6-km mean winds slowed from 7.2 to 4.1 m s^{-1}, while 0–6-km bulk shear remained largely unchanged (Table 1).

2) Hail accumulation and storm motion

This storm initially developed as a cluster of individual convective cells ~60 km northwest of the KFTG radar. Convection initiated along a westward-propagating boundary as evidenced by $Z > 50$ dBZ at the 0.5° elevation angle at 2345 UTC 4 June 2018 (see Fig. S1 in the online supplemental material). By 0010 UTC, the storm moved westward and began to exhibit supercell characteristics, including a Doppler velocity rotational couplet on the southwest side of the cell and a distinguishable hook echo. Ground observations confirmed an EF3 tornado at 0030 UTC[2] on 5 June. Between the time the storm first initiated and began to move westward, the radar indicated no hail accumulated on the ground within the isolated storm cell. We refer to the time between 2345 and 0010 UTC as the preaccumulation (PreA) period hereafter. For brevity, in this and following sections, accumulations were radar-derived (unless indicated as reported) and occurred within the isolated storm cell during the described period. Between 0010 and 0020 UTC, only trace amounts of hail (<3-cm depth) accumulated on the ground [henceforth referred to as the trace accumulation (TrcA) period]. During the TrcA period, the storm moved between 3 and 5 m s^{-1}. Hail accumulation increased starting at 0020 UTC, ranging between 3 and 8 cm until 0110 UTC [referred to as the moderate hail accumulation (ModA) period]. During this period, the storm speed reached a maximum of 8 m s^{-1}, which was faster than the TrcA period maximum speed. The storm eventually slowed down to 3 m s^{-1} at 0110 UTC, shortly before deeper accumulations were first derived.

The slowdown of the storm was strongly related to its motion uphill along the eastern edge of the Rocky Mountains. This strong relationship between terrain height and storm speed during the slowdown is indicated by a correlation of $r = -0.87$ (Fig. 6a). When compared to the entire analysis period between 2345 and 0300 UTC, the correlation between terrain height and storm speed is poor ($r = -0.16$, Fig. 6b). The poor correlation suggests the effects of terrain on storm motion may only be important when substantial changes in elevation occur. Thus, the rise in terrain, and subsequent slowdown of the storm, likely assisted in the increased hail accumulations by way of persistent accumulation over the same locations. We note the results shown thus far given during the TrcA and ModA periods agree with past studies in that storm motion is not strongly correlated to hail accumulation depth (Friedrich et al. 2019; Kumjian et al. 2019). However, this storm's transition from moderate to deep accumulations during a period of slow speed presents strong evidence that storm motion cannot always be disregarded.

[2] https://www.weather.gov/bou/StormSurveys.

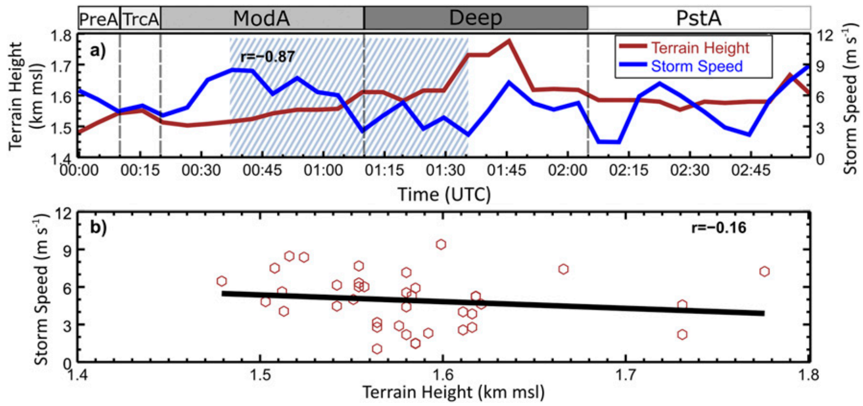

FIG. 6. (a) Time series of terrain height (dark red) and storm speed (blue). In the blue-hashed region, the correlation coefficient decreases to −0.87. (b) Scatterplot of the terrain height at the storm-centroid and the speed of the storm for each radar volume scan. The best-fit line is in black, and the Pearson correlation coefficient is at the top right. Accumulation periods are listed, separated by dashed lines.

Following the ModA period, a new period of increased hail accumulation (>8 cm) occurred between 0110 and 0205 UTC (referred to as the deep hail period). During this time, reported hail accumulations depths exceeded 14 cm and maximum hail diameters were about 5 cm in Lyons, Colorado (Fig. 5a). Also reported were hazardous driving conditions where drivers were stranded until hail was cleared from the road. The reported hail accumulations of >14 cm closely match the maximum radar-derived accumulations of approximately 17 cm at the same location (Fig. 7a, black square). When the storm produced its most intense hail accumulations (0110–0205 UTC), the storm speed was <5 m s^{-1}. However, an increase in storm speed from 3 to 7 m s^{-1} occurred between 0145 and 0152 UTC. At 0152 UTC, the storm speed returned to <5 m s^{-1} and hail accumulations began to decrease but still remained >8 cm until about 0205 UTC. Between 0205 and roughly 0330 UTC [referred to as the postaccumulation (PstA) period], the storm speed increased to >5 m s^{-1}, accumulations larger than 8 cm were no longer prevalent, and instead trace accumulations were predominantly derived.

3) HAIL PRODUCTION

Surface hail accumulation depends on the quantity of in-cloud hail production. In this study a storm's hail production was approximated by tracking the spatiotemporal evolution of accumulated VII and maximum accumulated flash extent density (henceforth abbreviated as flash extent density). Additionally, the temporal evolution of maximum storm-top divergence, storm-median flash footprint, and Z_{DR} column height above the 0°C isotherm were used to approximate in-cloud hail production for comparison to surface hail accumulations.

During the PreA period (2345–0010 UTC), accumulated VII and flash extent density increased to 50 kg m^{-2} and 5 flashes km^{-2} min^{-1}, respectively (Figs. 7b,c), while storm-top divergence increased to 110 m s^{-1} since the storm initiated (Fig. 8). Concurrently, storm-median flash footprint decreased from 60 to 20 km^2 (Fig. 8). All variables suggest hail production increased about 5–10 min before the storm began its TrcA period. Hail production continued to increase during the TrcA period as indicated by maximums in accumulated VII of 450 kg m^{-2}, flash extent density of 16 flashes km^{-2} min^{-1}, and storm-top divergence of 117 m s^{-1}. Notably, a Z_{DR} column extending to 2.7 km above the 0°C isotherm first became discernable during the transition between the TrcA and ModA periods. During the ModA period, trends in VII and lightning activity indicated oscillating rates of hail production. VII reduced to as little as 250 kg m^{-2}, and flash extent density to 8 flashes km^{-2} min^{-1}. Storm-top divergence also oscillated, where values variated between 95 and 115 m s^{-1}. Storm-median flash footprint exhibited distinct reductions at 0029, 0049, and 0105 UTC during the ModA period that were coincident with increased rates of accumulating hail. At 0030 UTC, the previously deep Z_{DR} column collapsed and a new Z_{DR} column initiated. Increases in Z_{DR} column height, accumulated VII, and flash extent density and a decrease in flash footprint occurred shortly before deep hail accumulations began (starting at 0110 UTC). Here, increases in Z_{DR} column height from 0.3 to 1.25 km, accumulated VII from 300 to 450 kg m^{-2}, and flash extent density from 8 to 12 flashes km^{-2} min^{-1} and a decrease in flash footprint from 45 to 30 km^2 were observed giving 0–10-min lead

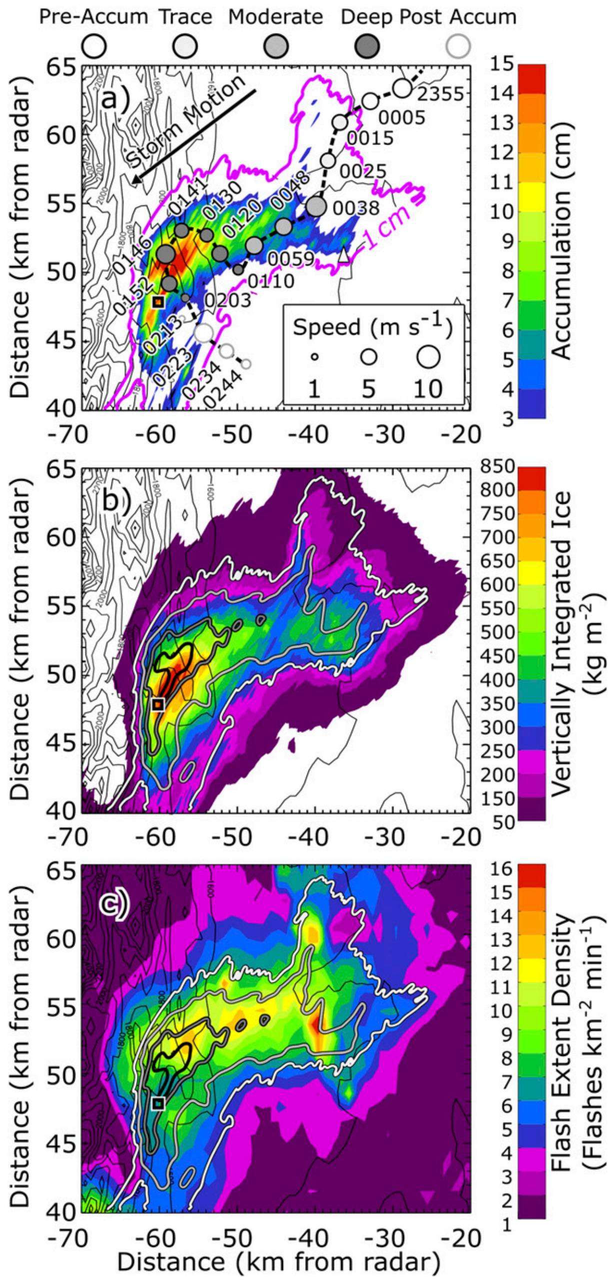

FIG. 7. Spatial distribution of (a) radar-derived hail accumulation, (b) radar-derived accumulated vertically integrated ice, and (c) maximum accumulated flash extent density, between 0000 and 0330 UTC near Lyons, CO. Data are based on observations by the KFTG radar and the COLMA. The black square at coordinates (−60, 48) indicates the hail depth report location. In (a), the magenta contour indicates accumulations of 1 cm, and filled contours are for accumulations greater than 3 cm. The dashed black line shows the storm track with gray circles indicating the centroid and speed of the storm at the UTC time shown. Solid thin black lines indicate terrain height. The white triangle indicates an area of interest discussed in the text. Lines in (b) and (c) indicate accumulations of 1 cm (white), 3 cm (light gray), 8 cm (gray), and 14 cm (black).

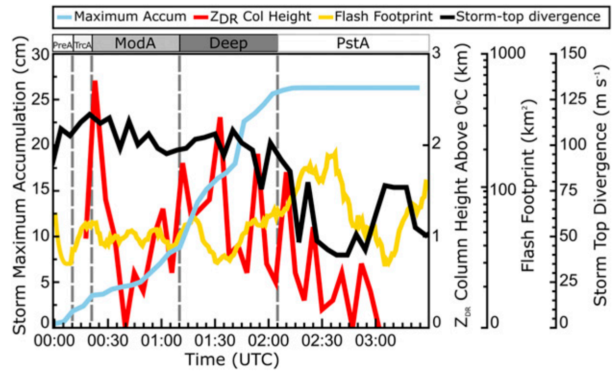

FIG. 8. Temporal evolution of storm-maximum hail accumulation (light blue), Z_{DR} column height above the 0°C isotherm (red), storm-top divergence (black), and storm-median flash footprint (orange). Accumulation periods are listed, separated by dashed lines.

time to deepening accumulations. During the deep hail period, the Z_{DR} column height varied between 0.5 and 2.3 km, but reached its maximum 10 min before the most intense increase in hail accumulation (0140–0200 UTC). Beginning at 0140 UTC, a rapid increase in accumulated VII, a peak in flash extent density and storm-top divergence, and a minimum in flash footprint provide similar advanced warning times for the most intense accumulations. During the PstA period, when maximum accumulations no longer increased, accumulated VII decreased from 800 to 50 kg m^{-2} and storm-top divergence from 105 to 40 m s^{-1}. The maximum Z_{DR} column height began to pulse with a decreasing trend. The pulses may be indicative of reinvigorated updrafts, or perhaps the collapse and initiation of new columns. Regardless, the decreasing trends suggest a decrease in hail production. However, flash extent density did not decrease nor did median flash footprint increase monotonically. At 0223 UTC, a peak in maximum flash extent density was observed, with an increase from 4 to 8 flashes km^{-2} min^{-1}, while at the same time storm-median flash footprint decreased from 150 to 110 km^2. These changes suggest the storm experienced a reinvigoration of updrafts that may explain the increased hail accumulations from scattered to ~7 cm between 0223 and 0234 UTC (Fig. 7a). As a result, it appears each in-cloud hail production proxy provided some utility in identifying when and where increases in hail accumulations occurred for this storm.

We note that enhanced in-cloud hail production did not always lead to enhanced hail accumulation. This is best shown when comparing observations at the start of the ModA period (0038 UTC, Fig. 7a near the 0038 centroid) and the start of the deep hail period (0110 UTC, in Fig. 7a nearest the 0120 centroid). At 0038 UTC, values of accumulated VII and lightning products suggest

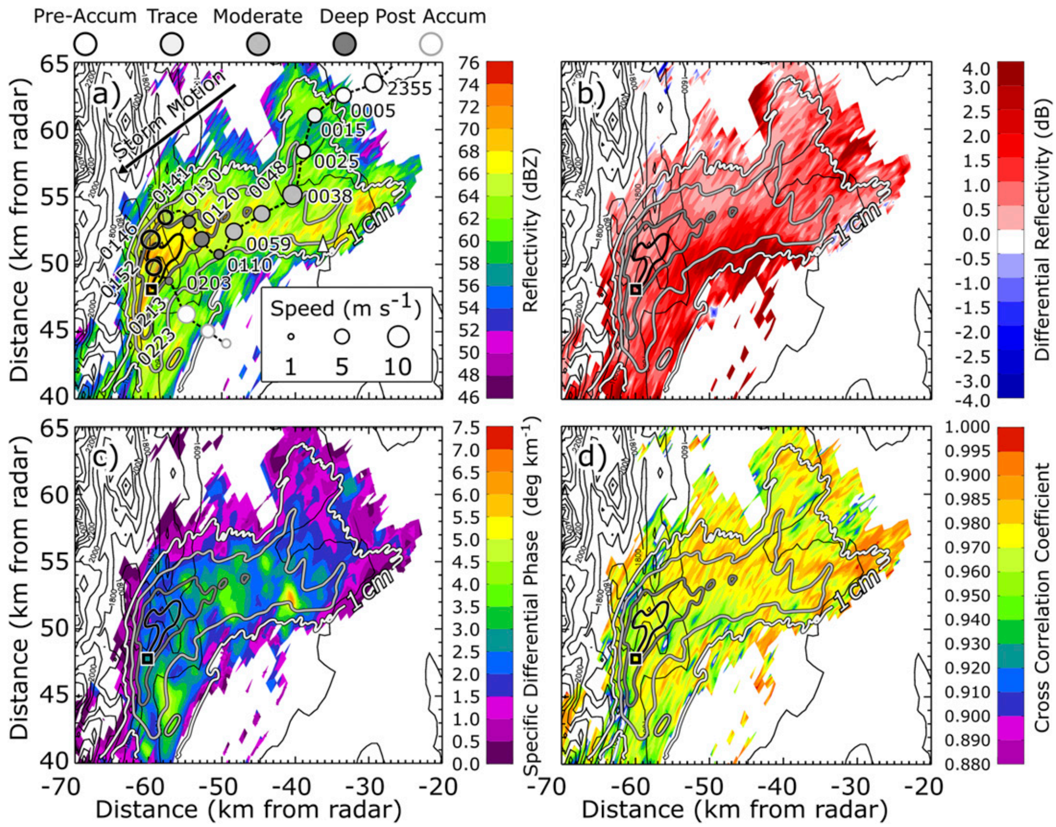

FIG. 9. As in Fig. 7, but showing spatial distributions of (a) maximum Z, (b) median Z_{DR}, (c) maximum K_{DP}, and (d) median R_{HV}. The lowest elevation scan (~0.5°) from the KFTG radar is used for this analysis, and only gates containing hail and hail with rain are included. Three circles between 0141 and 0152 UTC during the deep hail period are made transparent for easier inspection.

enhanced in-cloud hail production, similar to 0110 UTC. However, the radar-based hail accumulation indicates smaller accumulations (~5 cm difference) at 0038 UTC compared to 0110 UTC. This suggests that, while in-cloud hail production is important, accumulations also depend on other processes such as storm speed and hailstone melting. The combination of these processes will be discussed further in section 5.

4) HAILSTONE CHARACTERISTICS

In this section we show how utilizing the combination of maximum Z, maximum K_{DP}, median Z_{DR}, and median R_{HV} close to the surface, measured across all timesteps during the storm, helped identify areas that were experiencing or were about to experience hail accumulations. During the PreA period, maximum Z increased from <50 to 60 dBZ, maximum K_{DP} increased from 0.75° to 2.5° km^{-1}, and median Z_{DR} and R_{HV} remained primarily above 1.0 dB and 0.97, respectively (Fig. 9). These variables indicate that rain rates were increasing, but small melting hail may have been present for the first time since the storm initiated. During the TrcA period, maximum Z values ranged from 55 to predominately 60 dBZ with a general trend of increasing Z toward increasing accumulations. This is exemplified by noting enhanced Z of 65–70 dBZ occurred in the area 37 km west and 53 km north of the radar at 0038 UTC coincident with accumulations of approximately 5 cm (Figs. 7a, 9a, white triangle). During this time, maximum K_{DP} did not vary substantially compared to the PreA period. Minimum values of median Z_{DR} experienced decreasing trends, where areas of >4 dB were no longer observed. Contiguous areas of <0.5 dB became more prominent as well. This was particularly true north of 55 km and west of 35 km from the radar. Median R_{HV} ranged from 0.93 to 0.995, with no clear trend toward increasing accumulations. During this period, it is suggested that small melting hail and rain were still the dominant hydrometeors, but areas of increasing Z, paired with decreasing Z_{DR} and depressed R_{HV}, signify that at least some hailstones grew in size. It is possible that in isolated areas of $Z_{\mathrm{DR}} = 0$ dB, the reduction in Z_{DR} was indicative of tumbling hailstones larger than 2.5 cm in diameter. This is supported by noting that such large hailstones will shed their meltwater (Rasmussen and Heymsfield 1987; Ryzhkov et al. 2013a; Ortega et al. 2016), thereby preventing a buildup of water about their equators that can elevate Z_{DR} to >0 dB. During the ModA period, the dual-polarization radar products showed a progression of increasing maximum Z, relatively constant variability in median Z_{DR} and R_{HV}, and variations in maximum K_{DP}, leading up to the onset of the deep hail accumulation period. Given similar patterns, we surmise the hail in this region was similar in nature to the hail observed during the TrcA period.

During the deep hail period unique features appeared in the dual-polarization radar variables close to the surface (Fig. 9). First, maximum Z predominately exceeded 66 dBZ. Collocated with the large Z values were values of median Z_{DR} and R_{HV} that ranged between 0–1 dB and 0.93–0.97, respectively. These values suggest that the maximum hail size likely grew to >2.5 cm in diameter. While maximum Z, median Z_{DR}, and median R_{HV} underwent notable changes during this period, maximum K_{DP} remained primarily unchanged compared to the ModA period. This observation may be important since constant K_{DP} and increasing Z have been associated with increased hail fall rates when compared to rain rates (Balakrishnan and Zrnić 1990a; Ryzhkov et al. 2013a,b). Consequently, in the deep hail period, hail fall rates appear to have increased when compared to the ModA period. Therefore, for this storm, tracking the evolution of Z_{DR}, R_{HV}, Z, and K_{DP} was a useful tool in identifying areas of substantial hail accumulations. As the storm entered its PstA period, decreasing hail depths occurred when maximum Z rapidly decreased from 75 to <55 dBZ, median Z_{DR} increased to 2 dB, maximum K_{DP} increased to 5° km^{-1}, and median R_{HV} increased to above 0.980. These changes indicate a transition from hail-rain mixture to rain-dominating hydrometeors. A brief exception occurred when accumulations increased from scattered to about 7 cm at 0223 UTC. Here, similar patterns observed earlier in the storm in the dual-polarization evolution continued to help identify areas of accumulating hail.

b. *Characteristics of a storm producing moderate accumulations*

1) Preconvective local environment

The second storm we analyzed was an isolated thunderstorm within a larger multicellular complex that passed over Denver between 0426 and 0530 UTC and produced accumulations of 7 cm. The preconvective environment showed similar transitions as observed in the Lyons's environment (Fig. 4b, Table 1). Surface winds transitioned to easterly and midlevel moisture increased in the late afternoon. Consequently, precipitable water peaked at 21.2 mm. Most notable is the increase in CAPE at 2300 UTC of 2891 J kg^{-1}. The increase was a result of surface temperatures 14°C larger than those observed in the 1200 UTC sounding. A BRN of 104 in the afternoon suggests storms at this location were likely to be more disorganized than at locations with lesser BRN. The 0–6-km bulk shear remained largely unchanged from the 1200 UTC sounding, while 0–6-km mean winds slowed down from 9.0 to 3.6 m s^{-1} (Table 1).

2) Hail accumulation and storm motion

This storm initiated at 0426 UTC southwest of Denver, ~42 km west-southwest of KFTG, and moved northeastward (Fig. 10a). During the storm's PreA stage (0426–0451 UTC), the storm increased its speed from 4 to 11 m s^{-1}. When TrcA started at 0451 UTC, the storm slowed down to 8 m s^{-1}. The TrcA period lasted only 5 min, ending at 0456 UTC. During the period of ModA, between 0456 and 0518 UTC, the storm experienced a minimum speed of 4 m s^{-1} and changed in direction from northeast to southeast. Both the reduction in speed and change in direction were coincident with the time the deepest accumulations of up to 7 cm occurred. By 0518 UTC, the storm resumed its northeast heading and maintained a speed of >7 m s^{-1}. Here, the storm entered its PstA period, where trace hail accumulations were derived until about 0527 UTC, after which no hail accumulated.

A hail accumulation depth of 30–50 cm was estimated from a photo in a news article (Fig. 5b). The maximum reported hailstone diameter was ~2 cm (Mitchell 2015). The large discrepancy in the radar-derived hail accumulations and the photo-derived hail depth is most likely related to the hail drifts associated with heavy rainfall. Evidence of heavy rainfall was given by the news report, where icy rainwater was described as flowing downhill carrying trash bags and flooding at least one basement (Mitchell 2015). The news article itself indicated hail drifting, but additional inspection by the authors found that the intersection where the photo of the reported hail depth was taken resides in a topographic depression of roughly a few meters compared to its surroundings. Therefore, the local topography combined with reports of flooding provides a potential explanation for the discrepancy between the radar-derived and reported hail depths.

3) Hail production

As with the Lyons storm, changes in hail production provided some utility in identifying when and where accumulating hail occurred in this storm. During the

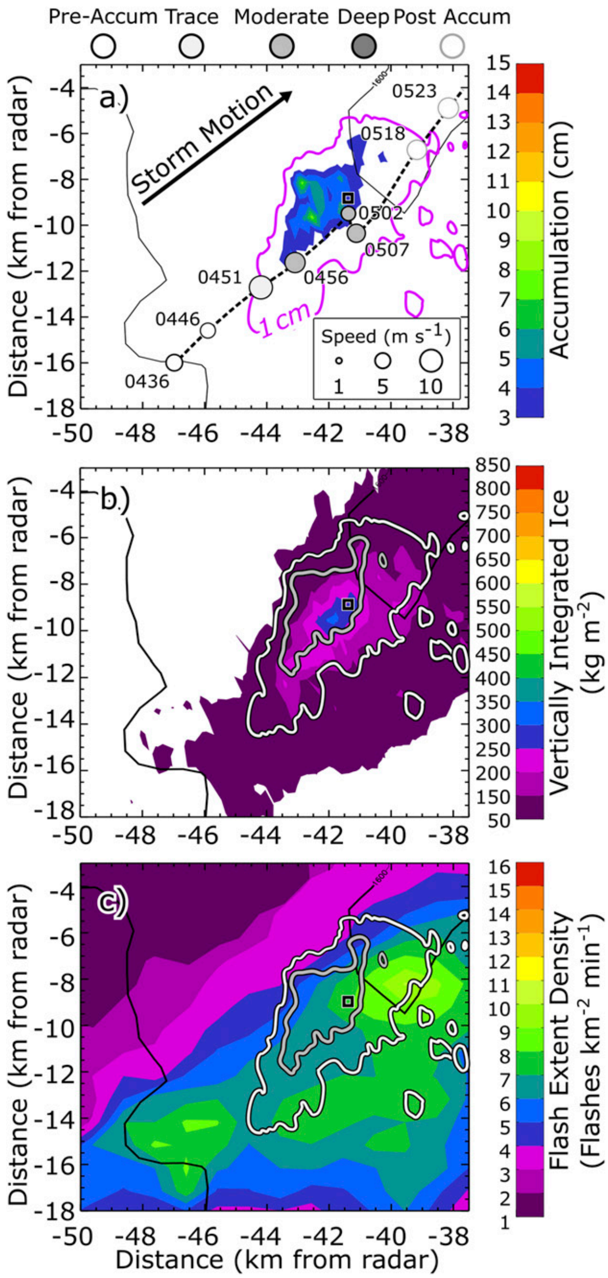

FIG. 10. As in Fig. 7, but using observations between 0430 and 0530 UTC near Denver, CO. Hail depth report is found at coordinates (−41.5, −8.5).

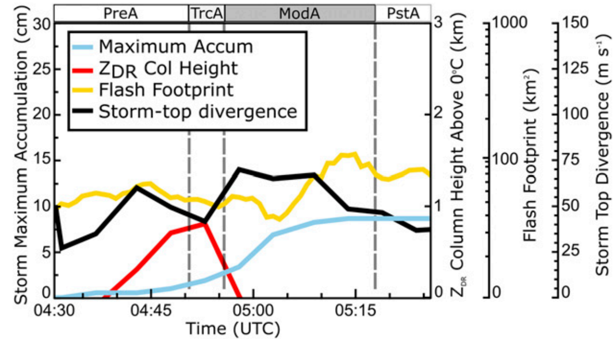

FIG. 11. As in Fig. 8, but using observations between 0430 and 0530 UTC near Denver, CO.

PreA period (0426–0451 UTC) an increase in accumulated VII from 0 to 50 kg m^{-2} and flash extent density from 4 to a maximum of 8 flashes km^{-2} min^{-1} (Figs. 10b,c) were observed beginning 10 min prior to the start of the TrcA period. Also observed during the PreA period was an increase in Z_{DR} column height above the 0°C isotherm from 0 to 0.7 km, storm-top divergence from 25 to 60 m s^{-1}, and a decrease in storm-median flash footprint from 60 to 40 km^2 (Fig. 11). The TrcA period only lasted 5 min and changes in accumulated VII and flash extent density failed to indicate increasing upcoming accumulations. Of interest though is the growth in the Z_{DR} column height above the 0°C isotherm to 0.8 km, an increase in storm-top divergence from 40 to 60 m s^{-1}, and a reduction in flash footprint from 40 to 35 km^2 during the TrcA hail period, each of which appeared to provide the best indication of increased hail production during this period. The Z_{DR} column, and possibly the updraft associated with it, disappeared concurrent with the start of the ModA period after 0456 UTC. As ModA began, accumulated VII increased to 200 kg m^{-2} while storm-top divergence increased to and then maintained roughly 70 m s^{-1}. Close to the storm's centroids, increased maximum flash extent densities were observed extending across wide areas on the southeastern edge of the deepest accumulations (Figs. 10c, Fig. S2). The enhanced flash extent density likely indicates newly formed updrafts, the strongest of which developed at 0502 UTC, and was located roughly 39 km west and 9 km south of the radar and slightly east of the centroid and hail accumulation area. At this location and time, maximum flash extent density up to 10 flashes km^{-2} min^{-1} was observed, while no new Z_{DR} columns were discernable from the radar data. The introduction of new updrafts is also inferable from the decrease in flash footprint at 0502 UTC from 50 to 30 km^2. At the same time, a nearby maximum in accumulated VII increased from 200 to 300 kg m^{-2}, where 300 kg m^{-2} was located within 1 km of the maximum accumulations (Figs. 10a,b). During the ModA period, VII, storm-top divergence, and lightning activity provided limited lead times of 0–5 min. At the onset of the PstA period at 0518 UTC when the storm began to accumulate <3 cm of additional hail, accumulated VII, storm-top divergence, and lightning activity began to indicate decreases in hail production. We note, during this period, a reduction in flash footprint at

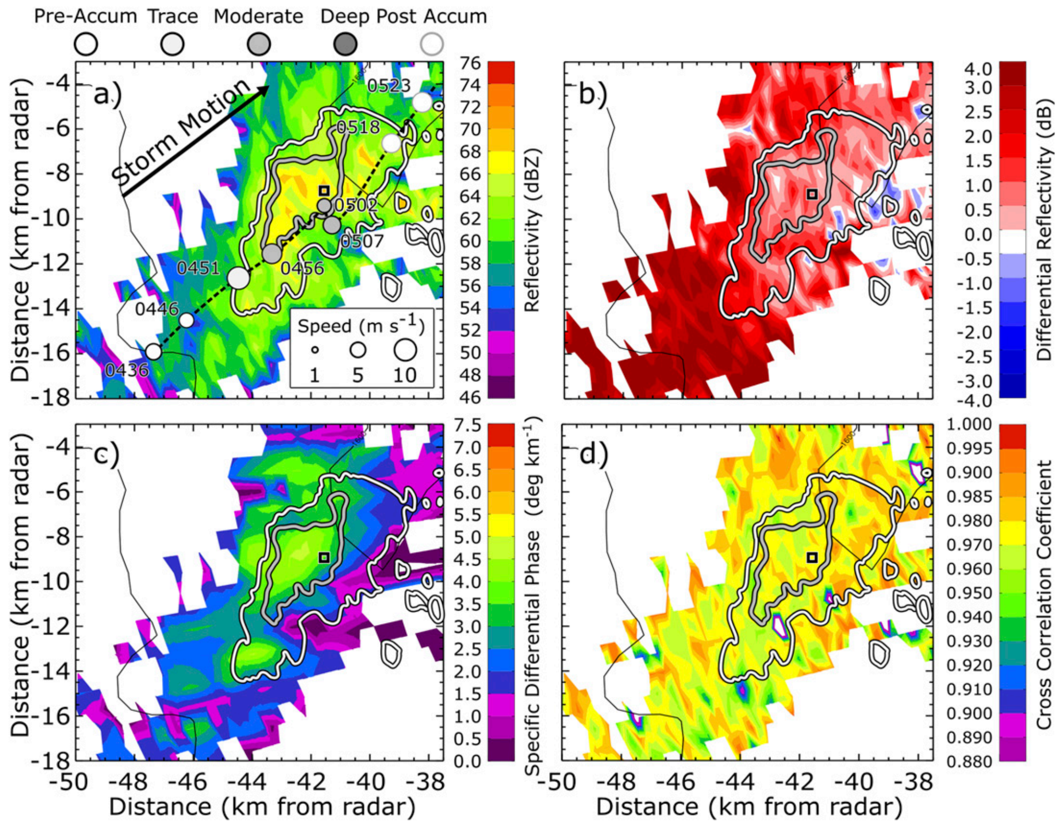

FIG. 12. As in Fig. 9, but using observations between 0430 and 0530 UTC near Denver, CO.

0518 UTC is associated with isolated areas of maximum accumulations of only ~1 cm.

4) Hailstone characteristics

Five minutes before TrcA began, maximum Z increased from 55 to 60 dBZ, median Z_{DR} decreased from 4 to 1.5 dB, maximum K_{DP} increased from 1° to 3.5° km^{-1}, and median R_{HV} varied between 0.93 and 0.98 (Fig. 12). While Z, Z_{DR}, and R_{HV} indicate hail was occurring in the lowest elevation scan, Z_{DR} paired with K_{DP} suggest that the predominant hydrometers were rain and small melting hail. With the start of the ModA period, Z values increased to 70 dBZ, Z_{DR} decreased to a minimum of −0.5 dB, and K_{DP} ranged around 4.0° km^{-1}. Based on these observations, substantial quantities of small melting hail may have been present; however, in conjunction with R_{HV} values ranging from 0.94 to 0.97, large melting hail might have occurred in areas of the maximum hail accumulations (Figs. 10a, 12). As the storm began to enter its PstA phase at 0518 UTC, both the large contiguous regions of Z of 65 dBZ and K_{DP} of 4.0° km^{-1} disappeared. Reflectivity Z continued to oscillate between 55 and 65 dBZ as the storm moved northeast, but hail accumulations did not exceed 3 cm after 0518 UTC. Differential reflectivity Z_{DR} and R_{HV} remained small. Each oscillated between 0 and 1.5 dB and 0.94 and 0.985, respectively. We suspect some hail was still falling in isolated areas. Still, the reduced Z and K_{DP} indicate reduced precipitation rates. We note that periodic areas of $Z_{DR} < -1.0$ dB were observed along the path of the updraft. These observations were possibly erroneous as a result of radar beam three-body scattering in the presence of large hail (Hubbert and Bringi 2000), or differential attenuation (Kumjian et al. 2019), both of which can artificially reduce Z_{DR}.

c. *Characteristics of a storm producing scattered hail accumulations*

1) Preconvective local environment

The third storm was an isolated thunderstorm within a larger multicellular complex that passed over ~43 km southwest of KFTG, near Littleton, Colorado, between 0600 and 0710 UTC. This storm produced scattered hail (Fig. 5c). The preconvective local environment was similar to the environment for the Denver storm (Fig. 4b, Table 1). This was not surprising given the storm's location was within 10 km (Fig. 1) and occurred within 1 h of the Denver storm. Because the 2300 UTC preconvection environments were similar, and for brevity, we refer the reader to section 4b(1) for an overview of this storm's convective potential.

While the preconvective environment was similar to the Denver storm, important to note is the characteristic near-storm environment is hypothesized to have differed across storms. Recall that the RAP-derived radiosonde data were taken 6 h prior to hail occurring at the Denver depth report location, and 7 h prior to the Littleton report. This suggests that the RAP data may not be representative of the then present wind shear and moisture profiles as well as hailstone embryo availability. This is especially true since adjacent convection may have altered each of the variables in different ways for each storm. However, these variables are impossible to quantify without better observations. The proposed hypothesis emphasizes the importance of studying the influences of near-storm environments in future research.

2) HAIL ACCUMULATION AND STORM MOTION

This storm initiated at 0615 UTC, 56 km southwest of KFTG, along a storm-produced outflow boundary. This storm initially moved to the northwest, but by 0625 UTC its motion began to follow the 500-hPa prevailing winds, where it changed direction to the northeast (Fig. 13a). Through the entire PreA period (0615 and 0636 UTC) storm motion was at a nearly constant speed of 6 $\mathrm{m\,s^{-1}}$. At the onset of TrcA, between 0636 and 0657 UTC, the storm slowed down from 6 to 4 $\mathrm{m\,s^{-1}}$. Hail depth reports of <3 cm during that time (Fig. 5c) match the radar-derived accumulations (Fig. 13a). The maximum hail size was reported to be 2 cm, not meeting the threshold for severe hail. Hail accumulations stopped at the hail depth report location at 0657 UTC. At the same time the storm speed increased from 4 to 7 $\mathrm{m\,s^{-1}}$. At 0657 UTC, the PstA period began as maximum accumulations never exceeded those derived at the hail depth report location. Reflectivity > 50 dBZ and isolated areas of trace accumulations continued to persist for another 33 min (0727 UTC) until the storm fully decayed.

3) HAIL PRODUCTION

Similar to the Lyons and Denver storms, the spatio-temporal evolution of the hail production proxies for the Littleton storm (accumulated VII, maximum accumulated flash extent density, storm-top divergence, storm-median flash footprint, and Z_{DR} column height above the 0°C isotherm) provided useful information to identify hail accumulations during this storm. Accumulated VII, flash extent density, storm-top divergence, and Z_{DR} column height increased from 0 to 50 $\mathrm{kg\,m^{-2}}$, from 1 to 5 flashes $\mathrm{km^{-2}\,min^{-1}}$, from 31 to 70 $\mathrm{m\,s^{-1}}$, and from 0.75 to 1.1 km, respectively, 10 min prior to the start of hail accumulations (Figs. 13b,c, 14). Storm-median flash footprint decreased from 60 to 30 $\mathrm{km^2}$ beginning 5 min prior to hail accumulations (Fig. 14). The combination of these six proxies indicate increased in-cloud hail production prior to hail accumulations. During the period of the most intense accumulations (0637–0641 UTC), accumulated VII never exceeded 50 $\mathrm{kg\,m^{-2}}$, both flash extent

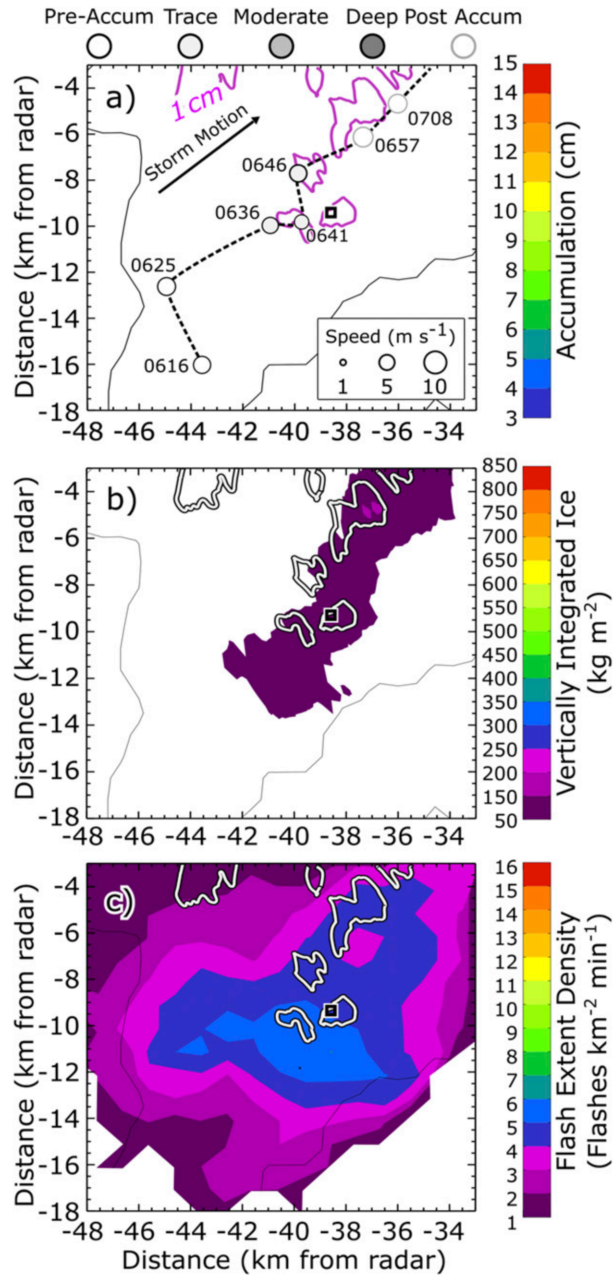

FIG. 13. As in Fig. 7, but using observations between 0600 and 0705 UTC near Littleton, CO. Hail depth report is found at coordinates (−38.5, −9).

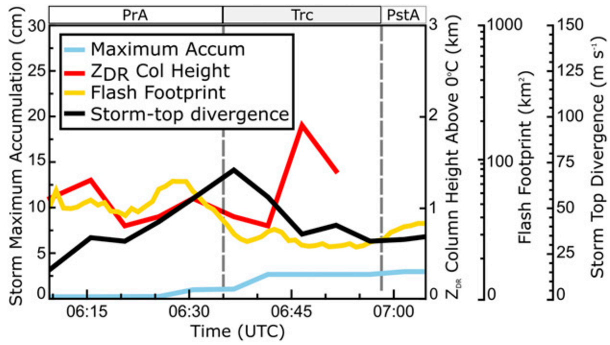

FIG. 14. As in Fig. 8, but using observations between 0600 and 0705 UTC near Littleton, CO.

density and storm-top divergence began to decrease, and storm-median flash footprint began to increase. A Z_{DR} column persisted through the TrcA period and disappeared at 0652 UTC as accumulations subsided. As trace accumulations continued after leaving the hail depth report location, neither accumulated VII, storm-top divergence, maximum flash extent density, nor median flash footprint showed remarkably different patterns from what has already been shown.

4) HAILSTONE CHARACTERISTICS

How the hailstone characteristics near the ground evolved in this storm gave only limited insight in how to identify scattered hail accumulations. After initiation, maximum Z increased from 50 dBZ (not shown) to 65 dBZ enhancing even to 70 dBZ in isolated areas about 10–15 min prior to trace accumulations (Fig. 15a). As maximum Z increased, median Z_{DR} decreased to 1 dB while maximum K_{DP} increased to 2° km^{-1} and median R_{HV} ranged from 0.94 to 0.97. As TrcA began, median Z_{DR} was primarily <1.5 dB, maximum K_{DP} reached up to 4.5° km^{-1}, and median R_{HV} decreased to a minimum of 0.96, respectively, in isolated areas (Figs. 15b–d). Of these four variables, only the decrease in median Z_{DR} best matched locations of hail accumulations. However, Z, Z_{DR}, K_{DP}, and R_{HV} strongly suggest that hail was small and melting in the areas near the hail depth report (Fig. 13a; black square). As the storm left the hail depth report area, maximum Z oscillated between 65 and 72 dBZ, with the largest values in areas of trace accumulations. In the same period, median Z_{DR} generally increased to 3 dB and median R_{HV} to above 0.96, but values near 0 dB and 0.94 were observed in subsequent areas of trace accumulation as well.

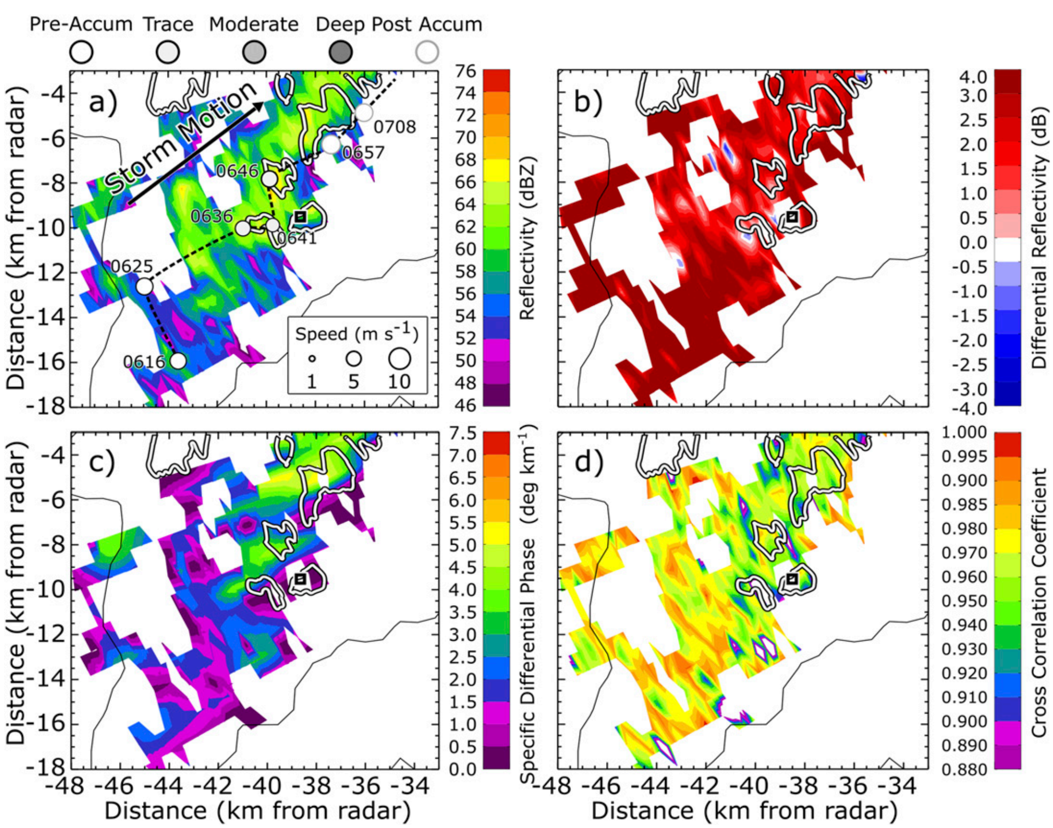

FIG. 15. As in Fig. 9, but using observations between 0600 and 0705 UTC near Littleton, CO.

Maximum K_{DP} of $5° km^{-1}$ was also observed in the subsequent area of trace accumulations. Here, we hypothesize nonaccumulating melting hail was falling, but the maximum hailstone size remained ambiguous. As the storm continued to move northeast, Z, Z_{DR}, and R_{HV} showed signs of continuous trace accumulation, while K_{DP} showed no such consistent value. As with the Denver storm, areas with $Z_{DR} < -4.0$ dB were likely associated with three-body scattering and/or differential attenuation.

5. Combination of storm characteristics and hail accumulation

In this section we highlight the complicated interaction between in-cloud hail production, storm speed, and hailstone melting, which can allow for better nowcasting potential. In each storm, changes in one of these parameters had potentially large consequences for the amount of hail that accumulated on the ground. The times and areas discussed hereafter and parameters indicating in-cloud hail production, storm speed, and hailstone melting are summarized in Table 2.

To support our hypothesis, we compare two areas within the Lyons storm that experienced similar in-cloud hail production but >10-cm difference in hail accumulation depth. The first area is located 37 km west and 53 km north of the radar at 0038 UTC coincident with accumulations of approximately 5 cm (Fig. 7a, white triangle). The second area is northeast of the hail depth report location, near 0130 UTC when accumulations first exceeded 14 cm (Fig. 7a; storm location near 0130 UTC). At each time, the storm underwent enhanced in-cloud hail production shown by high values of accumulated VII, that ranged 450–650 $kg m^{-2}$, flash extent densities of >10 flashes $km^{-2} min^{-1}$, storm-top divergences of $>100 m s^{-1}$, and storm-median flash footprints of $<40 km^2$ (Figs. 7c,d, 8; Table 2). Additionally, increased hail production is indicated by peaks in Z_{DR} column height > 1.75 km above 0°C approximately 15 min prior to deepening accumulations. However, differences in storm speed suggest that the faster moving period of the storm where the speed exceeded $8 m s^{-1}$ at 0038 UTC prevented accumulating hail while ample time to accumulate hail was provided during the slower-moving ($\leq 5 ms^{-1}$) period at 0130 UTC (Fig. 7a). During the period of faster storm motions at 0038 UTC, more melting was also indicated to be occurring, meaning deeper accumulations were less likely to occur. In this case, at 0038 UTC more rain was observed as K_{DP} was 3°–4° km^{-1} larger compared to 0130 UTC (Fig. 9c, Table 2). The larger water content at 0038 UTC suggests a favorable environment for melting. Therefore, the greater K_{DP} here can be explained by rapidly melting

TABLE 2. Radar- and lightning-derived parameters for the time and locations of the Lyons, Denver, and Littleton storms discussed in section 5: accumulated vertically integrated ice (VII), flash extent density, minimum flash footprint, maximum Z_{DR} column height, and storm-top divergence. Melting is listed as comparing qualitative melting impacts inferred from K_{DP} within the same storm (storm relative).

		In-cloud hail production parameters							
Storm name (maximum accumulation)	Time (UTC)	VII ($kg m^{-2}$)	Flash density (flashes $min^{-1} km^{-2}$)	Flash footprint (km^2)	Z_{DR} column height (km)	Storm-top divergence ($m s^{-1}$)	Storm speed ($m s^{-1}$)	Relative melting, K_{DP} (° km^{-1})	Radar-derived hail accumulation (cm)
Lyons (>20 cm)	0038	450	16	40	N/A	112	8	7	3
	0130	650	11	30	2.0	105	5	4	14
Denver (7 cm)	0446	50	8	50	0.7	50	11	3.5	1
	0507	300	10	40	N/A	65	4	4	7
Littleton (1 cm)	0636	50	5	25	0.8	70	4	4	1

or mostly melted hail, which resulted in less hail accumulation near 0038 UTC. With these results in mind, we note that not all increases in speed resulted in reduced hail accumulations. At 0146 UTC, accumulations of >14 cm occurred when an increase in storm speed was compensated by an increase in hail production and no significant change in hailstone melting.

A similar strategy was applied to identify the dominant process leading to hail accumulation in the Denver storm. The Denver storm initially produced no accumulation despite its speed of $<5\,\mathrm{m\,s^{-1}}$ (Fig. 10a). It was not until the storm experienced enhanced hail production and the storm slowed down and changed direction at 0502 UTC that the deepest hail accumulations (>3 cm) first appeared (Figs. 10, 11; Table 2). These accumulations were limited to <8 cm despite similar minimums in storm speed observed during the Lyons deep hail period. The smaller accumulations resulted in part due to weaker in-cloud hail production as evidenced in the radar derived and lightning patterns (Figs. 10–12). Still, moderate accumulations occurred in the presence of hailstone melting as evidenced by $Z > 60\,\mathrm{dB}Z$, $Z_{\mathrm{DR}} > 0$ dB, and K_{DP} of approximately $4^\circ\,\mathrm{km}^{-1}$ (Fig. 12, Table 2). Despite evidence of melting hailstones, observations of accumulations exceeding 3 cm alongside melting hailstones is not contradictory (e.g., Chappell and Rogers 1988; Schlatter and Doesken 2010; Kumjian et al. 2019). As a result, while large quantities of melting hail may have affected surface accumulations as suggested in the Lyons storm (Fig. 9a, area of $K_{\mathrm{DP}} > 6.5^\circ\,\mathrm{km}^{-1}$), the impact from melting remains more ambiguous than the effects from storm speed and hail production.

We conclude this discussion by the assessing the Littleton storm. The results discussed thus far support the conclusion that this storm's lack of accumulation was due in part to its relatively weak in-cloud hail production indicated by radar and lightning proxies, nearly constant speed and direction, and similar melting when compared to the Lyons and Denver storms (Figs. 13–15, Table 2). An interesting result is that when comparing Z_{DR} columns, the Z_{DR} column in the Littleton storm was more persistent and deeper than the column in the Denver storm. This suggests more hail production occurred in the Littleton storm, which does not explain the smaller accumulations. It is important to consider that identifying Z_{DR} columns can be difficult when hail causes three-body scattering or differential attenuation. Neither are important when observing the updraft in the Littleton storm as the updraft persisted to the southeast of the hail core. In contrast, during the Denver storm the updraft became obscured as it propagated around to the backside of the hail core (Fig. S2). Subsequently, the Denver storm may have possessed a persistent, deep, but undetectable Z_{DR} column.

6. Conclusions

In this study we compared in-cloud hail production, storm speed, and hailstone characteristics, including hailstone size and melting, of three hail-accumulating storms occurring on the same day along the Colorado Front Range with the goal of determining how these three variables affect surface hail accumulation. Our analysis of radar and lightning data showed a complicated interaction between the three variables and their spatial and temporal variations between storms and within storms that ultimately complicates hail depth forecasting. Predicting surface hail accumulations can only succeed when the processes are analyzed in concert. With respect to the hail accumulations derived in the three investigated storms, the major conclusions from this research are listed as follows:

1) The large-scale environmental setup, described by 500-hPa and surface maps and the morning operational sounding, showed conditions conducive to both multicellular and supercell thunderstorm development.
2) For the three storms, the local preconvective environments were too similar to provide valuable information to discriminate potential hail-accumulation depths.
3) In all three storms, storm speed alone provided little skill in identifying when or where hail accumulations would occur. Slow storm speed was not always indicative of increasing hail accumulations.
4) All three storms contained water-coated hailstones, suggesting melting was occurring, but not in sufficient magnitude to prevent all hail from reaching the ground at the hail depth report locations.
5) Accumulated VII provided skill in identifying areas of in-cloud hail production. Large VII values were often, but not always, associated with hail accumulations. In the storms analyzed, areas of VII > $400\,\mathrm{kg\,m^{-2}}$ were associated with accumulations > 14 cm except in cases where the speed of the storm exceeded $8\,\mathrm{m\,s^{-1}}$.
6) Each storm showed enhanced accumulated VII provides up to 5 min of lead time in advance of increases in accumulations.
7) The Lyons storm showed storm-top divergence exceeding $100\,\mathrm{m\,s^{-1}}$ and produced greater than 8 cm of accumulation. Storm-top divergences less than $70\,\mathrm{m\,s^{-1}}$ in the Denver and Littleton storms were associated with accumulations less than 8 cm.

8) In the storms analyzed, trends in storm-top divergence were potentially useful in identifying times when hail accumulations increased by providing up to 10 min of lead time.
9) Maximum accumulated flash extent density provided some skill in identifying areas of enhanced in-cloud hail production. In the storms analyzed, the largest hail accumulations occurred adjacent to the largest flash extent densities of each storm except in cases where the storm speed exceeded 8 m s^{-1}.
10) Storm-median flash footprint showed a valuable signal to identify times hail accumulations increased. In the storms analyzed, reductions in flash footprint often preceded or coincided with increasing accumulations.
11) Each storm showed increases in maximum accumulated flash extent density and decreases in storm-median flash footprint 5–15 min prior to increases in hail accumulations.
12) In each storm, Z_{DR} columns were observed during/prior to hail accumulations, but neither the height nor the pervasiveness was a standalone indicator of maximum accumulations.

Future research should focus on using a larger dataset for a similar analysis to assess how statistically significant these results are. From those results, one possible benefit may be developing an operational methodology to identifying areas of accumulating hail. Additionally, the larger dataset may give insight into the relatively unknown impacts of near-storm environments on hail accumulations. To answer this question storms must be selected by the criterion that appropriate instruments must be nearby storm initiation points. That criterion was unmet for this study to instead allow the assessment of three storms that occurred on the same day, each having hail depth reports to verify radar-derived accumulations. Ultimately, the results given by this study indicate any future research focused on hail accumulation needs to consider the complex interactions between hail production, storm speed, and hailstone melting when addressing why some storms produce hail accumulations and why others produce no accumulation at all.

Acknowledgments. Our gratitude goes out to the editor and three anonymous reviewers for their valuable input and suggestions. We also thank Bill Rison for providing the data collected by Colorado Lightning Mapping Array, and Eric Bruning for his assistance in operating the LMA Tools algorithm. We thank the University of Colorado for providing the Summit supercomputer (Anderson et al. 2017). Finally, we appreciate everyone that reported their hail depth and size. The research was supported under NOAA Award NA17OAR4320101 and National Science Foundation Division of Atmospheric and Geospace Sciences Award 1661583.

REFERENCES

Allen, J. T., M. R. Kumjian, C. J. Nixon, R. E. D. Jewell, B. T. Smith, and R. L. Thompson, 2020: Forecast parameters for US hail occurrence and size. *30th Conf. on Weather Analysis and Forecasting (WAF)/26th Conf. on Numerical Weather Prediction (NWP)*, Boston, MA, Amer. Meteor. Soc., 1A.4, https://ams.confex.com/ams/2020Annual/webprogram/Paper368490.html.

Anderson, J., P. Burns, D. Milroy, P. Ruprecht, T. Hauser, and H. J. Siegel, 2017: Deploying RMACC Summit: An HPC resource for the Rocky Mountain region. *PEARC17: Proc. Practice and Experience in Advanced Research Computing 2017 on Sustainability, Success and Impact*, New Orleans, LA, Association for Computing Machinery, 7 pp., https://doi.org/10.1145/3093338.3093379.

Baker, M. B., A. M. Blyth, H. J. Christian, J. Latham, K. L. Miller, and A. M. Gadian, 1999: Relationships between lightning activity and various thundercloud parameters: Satellite and modelling studies. *Atmos. Res.*, **51**, 221–236, https://doi.org/10.1016/S0169-8095(99)00009-5.

Balakrishnan, N., and D. S. Zrnić, 1990a: Estimation of rain and hail rates in mixed-phase precipitation. *J. Atmos. Sci.*, **47**, 565–583, https://doi.org/10.1175/1520-0469(1990)047<0565:EORAHR>2.0.CO;2.

——, and ——, 1990b: Use of polarization to characterize precipitation and discriminate large hail. *J. Atmos. Sci.*, **47**, 1525–1540, https://doi.org/10.1175/1520-0469(1990)047<1525:UOPTCP>2.0.CO;2.

Benjamin, S. G., and Coauthors, 2016: A North American hourly assimilation and model forecast cycle: The Rapid Refresh. *Mon. Wea. Rev.*, **144**, 1669–1694, https://doi.org/10.1175/MWR-D-15-0242.1.

Blair, S. F., D. R. Deroche, J. M. Boustead, J. W. Leighton, B. L. Barjenbruch, and W. P. Gargan, 2011: A radar-based assessment of the detectability of giant hail. *Electron. J. Severe Storms Meteor.*, **6** (7), https://ejssm.org/ojs/index.php/ejssm/article/viewArticle/87.

Brandes, E. A., J. Vivekanandan, J. D. Tuttle, and C. J. Kessinger, 1995: A study of thunderstorm microphysics with multiparameter radar and aircraft observations. *Mon. Wea. Rev.*, **123**, 3129–3143, https://doi.org/10.1175/1520-0493(1995)123<3129:ASOTMW>2.0.CO;2.

Bringi, V. N., D. A. Burrows, and S. M. Menon, 1991: Multiparameter radar and aircraft study of raindrop spectral evolution in warm-based clouds. *J. Appl. Meteor.*, **30**, 853–880, https://doi.org/10.1175/1520-0450(1991)030<0853:MRAASO>2.0.CO;2.

Brooks, H. E., J. W. Lee, and J. P. Craven, 2003: The spatial distribution of severe thunderstorm and tornado environments from global reanalysis data. *Atmos. Res.*, **67–68**, 73–94, https://doi.org/10.1016/S0169-8095(03)00045-0.

Brothers, M. D., E. C. Bruning, and E. R. Mansell, 2018: Investigating the relative contributions of charge deposition and turbulence in organizing charge within a thunderstorm. *J. Atmos. Sci.*, **75**, 3265–3284, https://doi.org/10.1175/JAS-D-18-0007.1.

Browning, K. A., 1964: Airflow and precipitation trajectories with severe local storms which travel to the right of the winds.

J. Atmos. Sci., **21**, 634–639, https://doi.org/10.1175/1520-0469(1964)021<0634:AAPTWS>2.0.CO;2.

——, and G. B. Foote, 1976: Airflow and hail growth in supercell storms and some implications for hail suppression. *Quart. J. Roy. Meteor. Soc.*, **102**, 499–533, https://doi.org/10.1002/qj.49710243303.

Bruning, E. C., 2015: lmatools: lmatools-v0.5z-stable. Accessed 8 August 2018, http://doi.org/10.5281/zenodo.32510.

——, and D. R. MacGorman, 2013: Theory and observations of controls on lightning flash size spectra. *J. Atmos. Sci.*, **70**, 4012–4029, https://doi.org/10.1175/JAS-D-12-0289.1.

Calhoun, K. M., D. R. MacGorman, C. L. Ziegler, and M. I. Biggerstaff, 2013: Evolution of lightning activity and storm charge relative to dual-Doppler analysis of a high-precipitation supercell storm. *Mon. Wea. Rev.*, **141**, 2199–2223, https://doi.org/10.1175/MWR-D-12-00258.1.

Carey, L. D., and S. A. Rutledge, 2000: The relationship between precipitation and lightning in tropical island convection: A C-band polarimetric study. *Mon. Wea. Rev.*, **128**, 2687–2710, https://doi.org/10.1175/1520-0493(2000)128<2687:TRBPAL>2.0.CO;2.

Chappell, C. F., and D. M. Rogers, 1988: Meteorological analysis of the Cheyenne, Wyoming, flash flood and hailstorm of 1 August 1985. NOAA Tech. Rep. ERL 435-FSL 1, 61 pp., https://repository.library.noaa.gov/view/noaa/11264/noaa_11264_DS1.pdf.

Conway, J. W., and D. S. Zrnić, 1993: A study of embryo production and hail growth using dual-Doppler and multiparameter radars. *Mon. Wea. Rev.*, **121**, 2511–2528, https://doi.org/10.1175/1520-0493(1993)121<2511:ASOEPA>2.0.CO;2.

Deierling, W., and W. A. Petersen, 2008: Total lightning activity as an indicator of updraft characteristics. *J. Geophys. Res.*, **113**, D16210, https://doi.org/10.1029/2007JD009598.

——, ——, J. Latham, S. Ellis, and H. J. Christian, 2008: The relationship between lightning activity and ice fluxes in thunderstorms. *J. Geophys. Res.*, **113**, D15210, https://doi.org/10.1029/2007JD009700.

Dennis, E. J., and M. R. Kumjian, 2017: The impact of vertical wind shear on hail growth in simulated supercells. *J. Atmos. Sci.*, **74**, 641–663, https://doi.org/10.1175/JAS-D-16-0066.1.

Doswell, C. A., 1987: The distinction between large-scale and mesoscale contribution to severe convection: A case study example. *Wea. Forecasting*, **2**, 3–16, https://doi.org/10.1175/1520-0434(1987)002<0003:TDBLSA>2.0.CO;2.

Durta, G., 2016: Heavy rain, hail hit northern Colorado; Week of storms to keep metro area cool and wet. KDVR, accessed 24 June 2018, https://kdvr.com/2016/04/25/week-of-storms-to-keep-us-cloudy-windy-cool-and-wet-for-next-several-days/.

Foote, G. B., 1984: A study of hail growth utilizing observed storm conditions. *J. Climate Appl. Meteor.*, **23**, 84–101, https://doi.org/10.1175/1520-0450(1984)023<0084:ASOHGU>2.0.CO;2.

Friedrich, K., and Coauthors, 2019: CHAT: The Colorado Hail Accumulation from Thunderstorms project. *Bull. Amer. Meteor. Soc.*, **100**, 459–471, https://doi.org/10.1175/BAMS-D-16-0277.1.

Gauthier, M. L., W. A. Petersen, L. D. Carey, and H. J. Christian Jr., 2006: Relationship between cloud-to-ground lightning and precipitation ice mass: A radar study over Houston. *Geophys. Res. Lett.*, **33**, L20803, https://doi.org/10.1029/2006GL027244.

Grant, L. D., and S. C. van den Heever, 2014: Microphysical and dynamical characteristics of low-precipitation and classic supercells. *J. Atmos. Sci.*, **71**, 2604–2624, https://doi.org/10.1175/JAS-D-13-0261.1.

Hubbert, J., and V. N. Bringi, 2000: The effects of three-body scattering on differential reflectivity signatures. *J. Atmos. Oceanic Technol.*, **17**, 51–61, https://doi.org/10.1175/1520-0426(2000)017<0051:TEOTBS>2.0.CO;2.

——, ——, L. D. Carey, and S. Bolen, 1998: CSU–CHILL polarimetric radar measurements from a severe hail storm in eastern Colorado. *J. Appl. Meteor.*, **37**, 749–775, https://doi.org/10.1175/1520-0450(1998)037<0749:CCPRMF>2.0.CO;2.

Johnson, A. W., and K. E. Sugden, 2014: Evaluation of sounding-derived thermodynamic and wind-related parameters associated with large hail events. *Electron. J. Severe Storms Meteor.*, **9** (5), https://ejssm.org/ojs/index.php/ejssm/article/viewArticle/137.

Johnson, J. T., P. L. MacKeen, A. Witt, E. D. Mitchell, G. J. Stumpf, M. D. Eilts, and K. W. Thomas, 1998: The Storm Cell Identification and Tracking algorithm: An enhanced WSR-88D algorithm. *Wea. Forecasting*, **13**, 263–276, https://doi.org/10.1175/1520-0434(1998)013<0263:TSCIAT>2.0.CO;2.

Kalina, E. A., K. Friedrich, B. Motta, W. Deierling, G. Stanno, and N. Rydell, 2016: Colorado plowable hailstorms: Synoptic weather, radar, and lightning characteristics. *Wea. Forecasting*, **31**, 663–693, https://doi.org/10.1175/WAF-D-15-0037.1.

Knight, C. A., and N. C. Knight, 2001: Hailstorms. *Severe Convective Storms, Meteor. Monogr.*, No. 50, Amer. Meteor. Soc., 223–249.

Kroosec, M., 2013: Impressive hail accumulation in Goito, North Italy—29 October 2013. Severe Weather Europe, accessed 10 December 2019, https://www.severe-weather.eu/recent-events/impressive-hail-accumulation-in-gioto-north-italy-october-29-2013/.

Kumjian, M. R., 2013: Principles and applications of dual-polarization weather radar. Part I: Description of the polarimetric radar variables. *J. Oper. Meteor.*, **1**, 226–242, https://doi.org/10.15191/nwajom.2013.0119.

——, and A. V. Ryzhkov, 2008: Polarimetric signatures in supercell thunderstorms. *J. Appl. Meteor. Climatol.*, **47**, 1940–1961, https://doi.org/10.1175/2007JAMC1874.1.

——, A. P. Khain, N. Benmoshe, E. Ilotoviz, A. V. Ryzhkov, and V. T. Phillips, 2014: The anatomy and physics of Z_{DR} columns: Investigating a polarimetric radar signature with a spectral bin microphysical model. *J. Appl. Meteor. Climatol.*, **53**, 1820–1843, https://doi.org/10.1175/JAMC-D-13-0354.1.

——, Z. J. Lebo, and A. M. Ward, 2019: Storms producing large accumulations of small hail. *J. Appl. Meteor. Climatol.*, **58**, 341–364, https://doi.org/10.1175/JAMC-D-18-0073.1.

Lawrence, H., 2017: Apocalyptic photos show sea of hail swamping cars in Argentina. *Independent*, accessed 5 May 2019, https://www.independent.co.uk/news/world/americas/argentina-hail-storm-terrifying-extreme-weather-cordoba-south-america-a8025056.html.

Lund, N. R., D. R. MacGorman, T. J. Schuur, M. I. Biggerstaff, and W. D. Rust, 2009: Relationships between lightning location and polarimetric radar signatures in a small mesoscale convective system. *Mon. Wea. Rev.*, **137**, 4151–4170, https://doi.org/10.1175/2009MWR2860.1.

Mitchell, K., 2015: One Denver block buried under up to 4 feet of hail. *Denver Post*, accessed 13 January 2019, https://www.denverpost.com/2015/06/05/one-denver-block-buried-under-up-to-4-feet-of-hail/.

Mosier, R. M., C. Schumacher, R. E. Orville, and L. D. Carey, 2011: Radar nowcasting of cloud-to-ground lightning over Houston, Texas. *Wea. Forecasting*, **26**, 199–212, https://doi.org/10.1175/2010WAF2222431.1.

Nelson, S. P., 1983: The influence of storm flow structure on hail growth. *J. Atmos. Sci.*, **40**, 1965–1983, https://doi.org/10.1175/1520-0469(1983)040<1965:TIOSFS>2.0.CO;2.

Ortega, K. L., J. M. Krause, and A. V. Ryzhkov, 2016: Polarimetric radar characteristics of melting hail. Part III: Validation of the algorithm for hail size discrimination. *J. Appl. Meteor. Climatol.*, **55**, 829–848, https://doi.org/10.1175/JAMC-D-15-0203.1.

Phillips, B. B., 1973: Precipitation characteristics of a sheared, moderate intensity, supercell-type Colorado thunderstorm. *J. Appl. Meteor.*, **12**, 1354–1363, https://doi.org/10.1175/1520-0450(1973)012<1354:PCOASM>2.0.CO;2.

Rasmussen, R. M., and A. J. Heymsfield, 1987: Melting and shedding of graupel and hail. Part II: Sensitivity study. *J. Atmos. Sci.*, **44**, 2764–2782, https://doi.org/10.1175/1520-0469(1987)044<2764:MASOGA>2.0.CO;2.

Rison, W., P. R. Krehbiel, R. J. Thomas, D. Rodeheffer, and B. Fuchs, 2012: The Colorado lightning mapping array. *2012 Fall Meeting*, San Francisco, CA, Amer. Geophys. Union, Abstract AE23B-0319.

Rutledge, S. A., E. R. Williams, and T. D. Keenan, 1992: The Down Under Doppler and Electricity Experiment (DUNDEE): Overview and preliminary results. *Bull. Amer. Meteor. Soc.*, **73**, 3–16, https://doi.org/10.1175/1520-0477(1992)073<0003:TDUDAE>2.0.CO;2.

Ryzhkov, A. V., S. E. Giangrande, and T. J. Schuur, 2005: Rainfall estimation with a polarimetric prototype of WSR-88D. *J. Appl. Meteor.*, **44**, 502–515, https://doi.org/10.1175/JAM2213.1.

——, M. R. Kumjian, S. M. Ganson, and A. P. Khain, 2013a: Polarimetric radar characteristics of melting hail. Part I: Theoretical simulations using spectral microphysical modeling. *J. Appl. Meteor. Climatol.*, **52**, 2849–2870, https://doi.org/10.1175/JAMC-D-13-073.1.

——, ——, ——, and P. Zhang, 2013b: Polarimetric radar characteristics of melting hail. Part II: Practical implications. *J. Appl. Meteor. Climatol.*, **52**, 2871–2886, https://doi.org/10.1175/JAMC-D-13-074.1.

Samenow, J., 2014: Two to three feet of hail crippled parts of Mexico City Sunday. *The Washington Post*, accessed 16 September 2019, https://www.washingtonpost.com/news/capital-weather-gang/wp/2014/08/19/two-to-three-feet-of-hail-crippled-parts-of-mexico-city-sunday/.

Saunders, C. P., 1993: A review of thunderstorm electrification processes. *J. Appl. Meteor.*, **32**, 642–655, https://doi.org/10.1175/1520-0450(1993)032<0642:AROTEP>2.0.CO;2.

Schlatter, T. W., and N. Doesken, 2010: Deep hail: Tracking an elusive phenomenon. *Weatherwise*, **63**, 35–41, https://doi.org/10.1080/00431672.2010.503841.

Schultz, C. J., L. D. Carey, E. V. Schultz, and R. J. Blakeslee, 2015: Insight into the kinematic and microphysical processes that control lightning jumps. *Wea. Forecasting*, **30**, 1591–1621, https://doi.org/10.1175/WAF-D-14-00147.1.

Snyder, J. C., A. V. Ryzhkov, M. R. Kumjian, A. P. Khain, and J. Picca, 2015: A Z_{DR} column detection algorithm to examine convective storm updrafts. *Wea. Forecasting*, **30**, 1819–1844, https://doi.org/10.1175/WAF-D-15-0068.1.

Takahashi, T., 1978: Riming electrification as a charge generation mechanism in thunderstorms. *J. Atmos. Sci.*, **35**, 1536–1548, https://doi.org/10.1175/1520-0469(1978)035<1536:REAACG>2.0.CO;2.

Tessendorf, S. A., L. J. Miller, K. C. Wiens, and S. A. Rutledge, 2005: The 29 June 2000 supercell observed during STEPS. Part I: Kinematics and microphysics. *J. Atmos. Sci.*, **62**, 4127–4150, https://doi.org/10.1175/JAS3585.1.

Vivekanandan, J., D. S. Zrnić, S. M. Ellis, R. Oye, A. V. Ryzhkov, and J. Straka, 1999: Cloud microphysics retrieval using S-band dual-polarization radar measurements. *Bull. Amer. Meteor. Soc.*, **80**, 381–388, https://doi.org/10.1175/1520-0477(1999)080<0381:CMRUSB>2.0.CO;2.

Wallace, R., K. Friedrich, E. A. Kalina, and P. Schlatter, 2019: Using operational radar to identify deep hail accumulations from thunderstorms. *Wea. Forecasting*, **34**, 133–150, https://doi.org/10.1175/WAF-D-18-0053.1.

Ward, A., M. Kumjian, M. J. Bunkers, S. W. Bieda III, and R. J. Simpson, 2018: Using polarimetric radar data to identify potentially hazardous hail accumulations. *34th Conf. on Environmental Information Processing Technologies*, Austin, TX, Amer. Meteor. Soc., 11B.1, https://ams.confex.com/ams/98Annual/webprogram/Paper326596.html.

Weisman, M. L., and J. B. Klemp, 1984: The structure and classification of numerically simulated convective storms in directionally varying wind shears. *Mon. Wea. Rev.*, **112**, 2479–2498, https://doi.org/10.1175/1520-0493(1984)112<2479:TSACON>2.0.CO;2.

Williams, E. R., and Coauthors, 1999: The behavior of total lightning activity in severe Florida thunderstorms. *Atmos. Res.*, **51**, 245–265, https://doi.org/10.1016/S0169-8095(99)00011-3.

Witt, A., and S. P. Nelson, 1991: The use of single Doppler radar for estimating maximum hailstone size. *J. Appl. Meteor.*, **30**, 425–431, https://doi.org/10.1175/1520-0450(1991)030<0425:TUOSDR>2.0.CO;2.

Zheng, D., and D. R. MacGorman, 2016: Characteristics of flash initiations in a supercell cluster with tornadoes. *Atmos. Res.*, **167**, 249–264, https://doi.org/10.1016/j.atmosres.2015.08.015.

Zrnić, D. S., N. Balakrishnan, C. L. Ziegler, V. N. Bringi, K. Aydin, and T. Matejka, 1993: Polarimetric signatures in the stratiform region of a mesoscale convective system. *J. Appl. Meteor.*, **32**, 678–693, https://doi.org/10.1175/1520-0450(1993)032<0678:PSITSR>2.0.CO;2.